RSC Advances

ROYAL SOCIETY OF CHEMISTRY

PAPER

View Article Online
View Journal | View Issue

Cite this: *RSC Adv.*, 2026, **16**, 13896

Structural and optical advances in Cu/Sr Co-doped ZnO nanomaterials for accelerated photocatalytic degradation of organic pollutant

Asif Ayub,[a] Abdul Rauf,*[a] Aqsa Anam,[a] Riyadh H. Alshammari,[b] Muhammad Zeshan Azam,[cd] Nida Ambreen[e] and Muhammad Arshad *[a]

Rational co-doping of ZnO with electronically active and lattice-modifying elements has proven to be an effective strategy to enhance photocatalytic efficiency through simultaneous band-structure tuning and defect engineering. Herein, Cu/Sr co-doped ZnO nanomaterials ($Zn_{1-(x+y)}Cu_xSr_yO$, with x = 0.03, 0.06, 0.09 and y = 0.04) were synthesized *via* a one-step chemical precipitation method under controlled pH and thermal treatment. X-ray diffraction (XRD) confirmed the retention of the wurtzite ZnO structure with systematic lattice expansion, indicating successful substitutional incorporation of Cu^{2+} and Sr^{2+} ions. Optical absorption measurements showed a red-shift of the absorption edge and reduced band-gap energy (~2.98 eV) compared with pristine ZnO (~3.20 eV). Under simulated solar irradiation (678.32 W m^{-2}), the co-doped ZnO exhibited markedly enhanced photocatalytic degradation of Congo red (~97% removal within 90 min at a catalyst dose of 15 mg), following pseudo-first-order kinetics (k = 0.040 min^{-1}, R^2 = 0.992). Photoluminescence (PL) quenching, radical scavenger experiments, and reduced charge transfer resistance from electrochemical impedance spectroscopy (EIS) collectively indicate improved charge separation and suppressed recombination in the co-doped system. Furthermore, the photocatalyst retained its structural integrity and photocatalytic efficiency over five consecutive cycles, as confirmed by post-reaction XRD analysis. These findings demonstrate that synergistic Cu/Sr co-doping effectively tuned the structure–property–performance relationship in ZnO, leading to enhanced and stable photocatalytic activity.

Received 6th November 2025
Accepted 5th March 2026

DOI: 10.1039/d5ra08566g

rsc.li/rsc-advances

1 Introduction

The continuous discharge of dye-laden wastewater from textile, pharmaceutical, cosmetic, and food industries poses a serious environmental concern due to the high persistence, toxicity, and potential carcinogenicity of synthetic dyes.[1,2] Congo red (CR), a water-soluble anionic azo dye, can undergo reductive cleavage to form benzidine-type intermediates, which are well known for their mutagenic and carcinogenic effects. These byproducts exhibit a reported benzidine activity level of approximately 0.108 ppm per day.[3]

Conventional wastewater treatment and separation techniques face considerable challenges and limitations, and often lead to partial transformation rather than complete mineralization of such pollutants. In this context, advanced oxidation processes (AOPs) offer promising potential for the complete degradation of highly stable CR molecules in aqueous media.[4–6] Heterogeneous photocatalysts such as TiO_2 (ref. 7) ZnO[8] $BiVO_4$ (ref. 9) Fe_2O_3 (ref. 10) WO_3 (ref. 11) MnO_4 (ref. 12) SnO_2 (ref. 13) CeO_2 (ref. 14) and ZnS[15] have been widely investigated for wastewater treatment.

ZnO, a n-type semiconductor with a wurtzite crystal structure, has gained significant attention owing to its favourable properties, including strong photochemical activity, good electrical characteristics, chemical stability and non-toxicity.[16] Despite these advantages, its photocatalytic application remains limited due to its wide band gap (>3.0 eV), which restricts photon absorption primarily to the ultraviolet region (<380 nm),[17] accounting for only about 5% of the solar spectrum.[18] Furthermore, rapid electron–hole recombination restricts the availability of charge carriers for redox reactions. Consequently, current research efforts are concentrated on enhancing the catalytic performance of ZnO through various strategies such as cationic and anionic doping, morphological

[a]*Institute of Chemistry, The Islamia University of Bahawalpur, Baghdad-ul-Jadeed Campus, Bahawalpur 63100, Pakistan. E-mail: abdul.rauf@iub.edu.pk; muhammad.arshad@iub.edu.pk*

[b]*Department of Chemistry, College of Science, King Saud University, Riyadh 11451, Saudi Arabia*

[c]*School of Chemical Engineering and Technology, Tianjin University, Tianjin 300350, China*

[d]*Department of Chemical Engineering, Wah Engineering College, University of Wah, 47040, Pakistan*

[e]*Department of Chemistry, Abdul Wali Khan University Mardan, Mardan, KPK 23200, Pakistan*

engineering, synthesis of hybrid nanomaterials, and surface modification techniques.[19]

Elemental doping with transition metals and alkaline earth metals is an effective way to tailor the structural and electronic properties of ZnO and ultimately enhance its photocatalytic activity.[20–22] In recent years, ZnO doped individually with Sr^{2+}, has been explored to induce lattice distortion and defect formation due to its large ionic radius compared with Zn^{2+}, leading to the creation of oxygen vacancies.[23,24] However, transition metals such as iron, chromium, manganese, tungsten, and copper have also been widely used to engineer the electronic properties of semiconductor materials by modifying the band gap energy, band edge position, Fermi level, and d-orbitals configuration. The partially filled d-orbital of these metals introduces intermediate energy states within the band structure, facilitates bandgap narrowing, and induces a redshift in optical absorption. This strategic modification enhances visible-light harvesting, and improve photocatalytic efficiency under solar irradiation.[25] For instance, Hossain *et al.*, achieved 99% photocatalytic degradation efficiency of Cu-doped hydroxyapatite.[26] In another study, A. K. Manna *et al.* reported 73% degradation efficiency for MB using 3% Cu-doped ZnO, synthesized *via* one step electrodeposition method.[27] Similarly, Rahman *et al.*[28] demonstrated a 95.17% degradation efficiency of the Cu-doped ZnO nanoparticles under simulated sunlight.

Recent studies have demonstrated that co-doping in ZnO, when carefully optimized, has shown better performance over single-element doping due to synergistic effects that improve both dopant solubility and charge carrier mobility.[29] Several co-doping combinations have been investigated for ZnO, such as La/Cu,[30] Ca/Mg,[29] Al/La,[31] Al/Ni,[32] C/Ce,[33] Ce/Gd,[34] Ni/Cd.[35] However, Cu/Sr co-doping has not yet been explored for tuning the structural and optical properties of ZnO.

Inspired by the above discussion, the present study reports the synthesis of Cu/Sr co-doped ZnO (CSZO) nanomaterials *via* chemical precipitation method, a comparatively simple and cost-effective technique. To the best of our knowledge, no prior studies have explored the combined effect of Cu (transition metal) and Sr (alkaline earth metal) as co-dopants in tuning the structural, morphological, optical, electrochemical and thermal properties of ZnO. Furthermore, the photocatalytic degradation efficiency of the synthesized materials wasinvestigated under visible-light irradiation against the organic dye CR as model organic pollutant. Key operational parameters such as solution pH, catalyst dose, and initial CR concentration were rigorously optimized to improve degradation performance. In addition, radical trapping experiments were performed to identify the dominant reactive species involved and to gain insight into the possible photocatalytic degradation mechanism.

2 Experimental section

2.1 Required materials

All the chemicals were of analytical grade and used as received without further purification. Zinc acetate dihydrate ($Zn(CH_3COO)_2 \cdot 2H_2O$, ≥99%), strontium chloride hexahydrate ($SrCl_2 \cdot 6H_2O$, ≥99%), copper(II) chloride dihydrate ($CuCl_2 \cdot 2H_2O$, ≥99%), Congo red, disodium ethylenediaminetetraacetate (EDTA-2Na, ≥99%), *p*-benzoquinone (*p*-BQ, ≥98%), isopropyl alcohol (IPA, ≥99.9%), silver nitrate ($AgNO_3$, ≥99.9%), citric

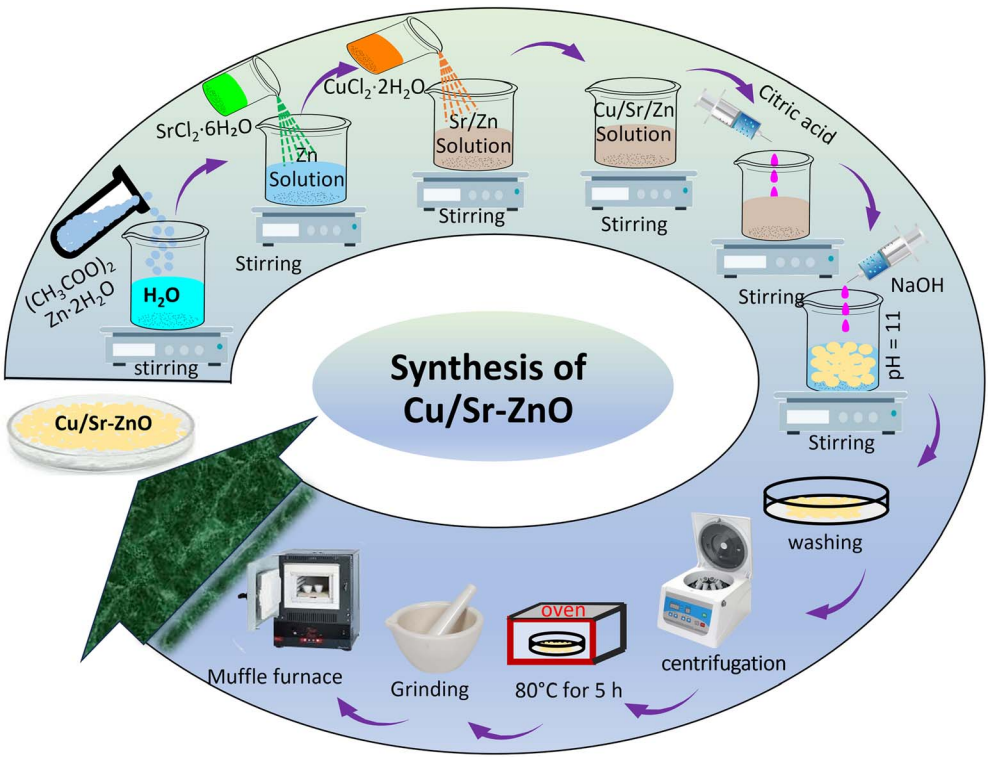

Scheme 1 Synthesis of CSZO *via* chemical precipitation method.

acid ($C_6H_8O_7$, ≥99.5%), sodium hydroxide (NaOH, ≥98%), and hydrochloric acid (HCl, 37%) were purchased from Sigma-Aldrich (USA) and Merck (Germany).

2.2 Synthesis of catalysts

Pristine ZnO (ZO), Sr-doped ZnO (SZO), and Cu/Sr co-doped ZnO (CSZO) nanomaterials were synthesized *via* one-step chemical precipitation method, as illustrated in Scheme 1. For pristine ZO synthesis, 10.97 g of $Zn(CH_3COO)_2 \cdot 2H_2O$ was mixed with 50 mL of double-distilled (DD) water to obtain a 1.0 M solution. The solution was homogenized by stirring at 600 rpm at room temperature for 10 min. Subsequently, 0.5 g of citric acid was added as a chelating agent while maintaining constant agitation. The pH of the solution was then gradually adjusted to 11 by dropwise addition of freshly prepared 1.0 M NaOH solution under continuous stirring for 40 min. The alkaline pH was selected to promote the complete precipitation of $Zn(OH)_2$, which subsequently transforms into ZnO upon thermal treatment. The resulting precipitates were collected, washed repeatedly with DD water to remove residual ions, and dried at 80 °C for 5 h in a hot-air oven. The dried powder was calcined at 550 °C for 2 h in air using a muffle furnace (heating rate 5 °C min^{-1}). Finally, the calcined product was ground into fine powder of ZO nanomaterial. For SZO synthesis, a similar protocol was followed, except that 0.04 M $SrCl_2 \cdot 6H_2O$ (0.53 g in 50 mL) was added into 0.96 M Zn precursor solution prior to precipitation. For Cu/Sr co-doped ZnO, appropriate molar ratios of $Zn(CH_3COO)_2 \cdot 2H_2O$, $SrCl_2 \cdot 6H_2O$ ($x = 0.04$), and $CuCl_2 \cdot 2H_2O$ ($y = 0.03$, 0.06, 0.09) were prepared separately in 50 mL of water and stirred for 30 min each. After that, Sr salt solution was first poured into the zinc salt solution, and stirred for further 30 min. Next, Cu salt solution was also added into the above mixture and further stirred (600 rpm) for 30 min. Citric acid (0.5 g) was added as capping agent and precipitation was initiated by adjusting the pH of the reaction mixture to 11 using a freshly prepared 1.0 M NaOH solution. The resulting precipitates were collected, thoroughly washed with DD water, dried and calcined following the same procedure as adopted for pristine ZnO. The synthesized samples were denoted as CSZO-1, CSZO-2, and CSZO-3, and their detailed compositions are summarized in Table 1.

2.3 Characterization of nanomaterials

Structural properties and crystalline size of the synthesised nanomaterials were analysed by XRD, using PANalytical X'Pert PRO MPD, with Cu Kα radiation ($\lambda = 1.54$ Å) operated at 40 kV. Data were recorded over 2θ range of 10–80° with scan rate of 0.02° s^{-1}. Functional groups and metal oxygen bonding were analysed by Fourier Transform Infrared (FTIR) spectroscopy by utilizing Shimadzu-MIRacle 10, in the wavelength range of 400–4000 cm^{-1}. X-ray photoelectron spectroscopy (XPS) was used to probe the surface chemical state and elemental composition using Thermo Scientific instrument (UK) with Al Kα X-ray source (1486.6 eV). Morphological features of the catalysts were examined using scanning electron microscopy (SEM) with JEOL JSM-7100F, 15 kV accelerating voltage and transmission electron microscopy (TEM) using JEOL JEM-2100 Plus, operated at 200 kV. Porosity and specific surface area of the samples were evaluated using N_2 adsorption–desorption isotherm (BET method), performed on a NOVA touch LX analyser after degassing the samples at 150 °C for 6 h. A UV-vis spectrophotometer (PerkinElmer Lambda 365) in the wavelength range of 200–800 nm was used to investigate the optical properties of the samples. Photoluminescence (PL) measurements were carried out using Jasco FP-8200 spectrofluorimeter. Thermal stability was examined using thermogravimetric analysis (TGA) (Hitachi Model-7300) under nitrogen atmosphere at a heating rate of 10 °C min^{-1}.

2.4 Photocatalytic experiment

Photocatalytic efficiency of both doped and undoped nanomaterials was assessed through the photodegradation of CR. Initially, 5 mg of catalyst was added in 50 mL of a 10 ppm dye solution. The solution mixture was then stirred magnetically in the dark until it achieved adsorption–desorption equilibrium. Subsequently, it was irradiated under visible-light provided by 500 W Xe lamp equipped with a 400 nm UV cut-off filter, positioned 15 cm from the reactor. The light intensity at the solution surface was measured using calibrated radiometer and the irradiance was recorded as 678.32 W m^{-2}. The reaction temperature was kept constant at 25 °C using a water-circulating jacket. After every 15 min, 2 mL of aliquots were collected and transferred to a cuvette for analysis. The catalyst particles from the aliquots were separated by centrifugation. The residual dye concentration was analysed using a UV-vis spectrophotometer in the wavelength range of 200–800 nm. All the experiments were performed in triplicate, and results are presented as mean values ± standard deviation. The photodegradation efficiency η (%) was calculated using eqn (1)

$$\eta(\%) = \frac{C_0 - C_t}{C_0} \times 100 \quad (1)$$

Table 1 Samples formulation with a different doping concentration, with sample codes

			Precursor content			
Sr no	Sample codes	Samples	Zn precursor (M)	Cu precursor (x) (M)	Sr precursor (y) (M)	Doping level
1	ZO	ZnO	1.00			$Zn_{1.00}O$
2	SZO	Sr doped ZnO	0.96		0.04 M	$Zn_{0.96}Sr_{0.04}O$
3	CSZO-1	Cu/Sr co-doped ZnO	0.93	0.03 M	0.04 M	$Zn_{0.093}Cu_{0.03}Sr_{0.04}O$
4	CSZO-2	Cu/Sr co-doped ZnO	0.90	0.06 M	0.04 M	$Zn_{0.090}Cu_{0.06}Sr_{0.04}O$
5	CSZO-3	Cu/Sr co-doped ZnO	0.87	0.09 M	0.04 M	$Zn_{0.087}Cu_{0.09}Sr_{0.04}O$

Here, C_0 and C_t denote the initial concentration of dye solution before irradiation and its concentration after irradiation at a specific time t, respectively.

Additionally, the role of reactive species like electrons (e^-), holes (h^+), hydroxyl radicals ($\cdot OH$), and superoxide radicals ($O_2^{\cdot -}$) was investigated under similar experimental conditions. Specific scavengers were employed to selectively suppress each species: IPA (10 mM) for $\cdot OH$, $AgNO_3$ (1 mM) for e^-, EDTA (1 mM) for h^+, and *p*-BQ (1 mM) for $O_2^{\cdot -}$. This approach allowed the identification of their respective contribution to the photocatalytic degradation of CR. Control experiments without scavengers were also performed to ensure mechanistic validity.

3 Results and discussion

3.1 Structural analysis

To investigate the effects of Sr^{2+} and Cu^{2+} doping on phase purity and structural properties of the ZnO lattice, XRD analysis of ZO, SZO, CSZO-1, CSZO-2, and CSZO-3 was performed in the 2θ range of 10–80° as shown in Fig. 1a. The diffraction peaks of ZO were observed at 2θ values of 31.89°, 34.53°, 36.33°, 47.67°, 56.71°, 62.96° and 66.49°, 68.03°, 69.16°, 72.74°, 77.08° which are consistent with the (100), (002), (101), (102), (110), (103), (200), (112), (201) lattice planes, respectively. All characteristic diffraction peaks observed in the ZO sample correspond to the hexagonal wurtzite structure of ZnO (JCPDS no. 36-1451).[36]

The diffraction patterns of SZO, CSZO-1, CSZO-2, and CSZO-3 catalysts are consistent with that of ZO, which supports the purity of the synthesized samples and rules out the presence of secondary phases of SrO and CuO in the crystal lattice. The weak peaks near 25° and 43° do not coincide with the full set of characteristic CuO and SrO reflections, indicating no detectable secondary phases within the XRD detection limit. A shift of diffraction peaks toward lower 2θ value is observed upon Sr^{2+} doping, as depicted in the enlarged view of XRD patterns (Fig. 1b). This shift can be attributed to lattice expansion caused by substitution of larger Sr^{2+} ions (0.118 nm) at Zn^{2+} sites (0.074 nm), leading to an increase in the lattice parameters and lattice distortion. In case of co-doping, a slight peak shift toward lower 2θ values is also observed, which can be attributed to (i) strain produced in ZO lattice because of mismatch in ionic radii among Sr^{2+}, Cu^{2+} (0.073 nm) and Zn^{2+}, (ii) dopant induced lattice strain and (iii) changes in lattice spacing. Ghorbali *et al.* have observed a similar doping effect of In and Cu in ZnO nanostructures.[37] These shifts in peak positions indicate effective doping and co-doping without disrupting the ZO crystal structure. Fig. 1b also illustrates that Sr^{2+} doping reduces the peak intensity, while co-doping with Cu^{2+} enhances the peak intensity at moderate Cu concentration, followed by a slight reduction at higher dopant levels. Lower peak intensities in doped materials suggest lower crystallinity in the sample due to lattice strain and distortion, while higher peak intensity in co-doped samples signifies a well-crystallized structure. The average crystallite size was calculated by Debye–Scherrer's equation[38] as shown below.

$$D = \frac{K\lambda}{\beta \cos\theta} \tag{2}$$

where D, k, λ, β, and θ represent the avereage crystallite size, shape factor (0.9), wavelength of X-ray source, full width at half maxima (FWHM), and Bragg angle, respectively.

Although the Debye–Scherrer method provides a convenient way to estimate crystallite size, but instrumental effects and residual stress can influence the peak broadening. To separate sample-induced broadening from instrument-related effects, instrumental broadening was corrected using a standard silicon reference sample with a well-defined (111) diffraction plane. The instrumental contribution was subtracted from the experimentally observed peak width to obtain corrected FWHM (β_{hkl}) values of the co-doped samples, as described in eqn (3). The corrected β_{hkl} values were subsequently employed to estimate the average crystallite size using Debye–Scherrer eqn (2).

$$\beta_{hkl} = \sqrt{(\beta_{obs})^2 - (\beta_{inst})^2} \tag{3}$$

The crystallite size of the synthesized samples was found to be in the range of 29–46 nm. The dislocation density (δ) of the synthesized samples was calculated using eqn (4), and the results are summarized in Table 2.

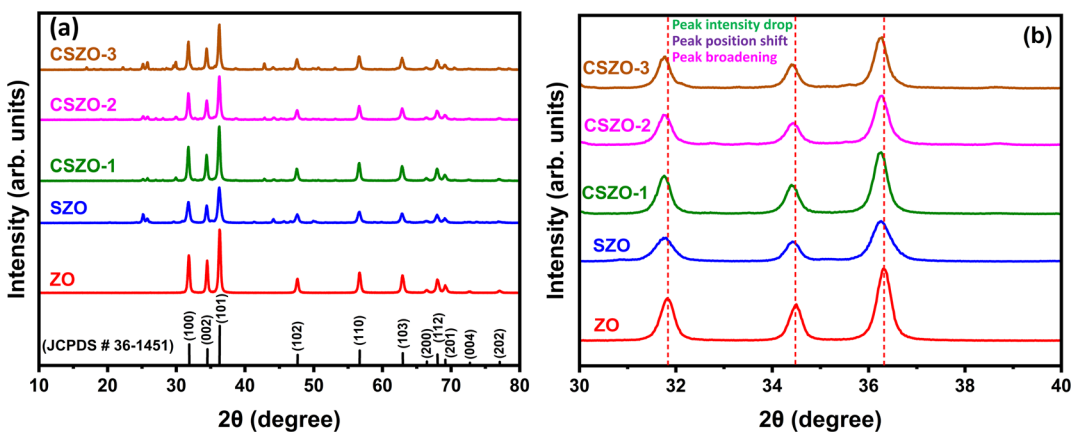

Fig. 1 (a) XRD pattern (b) enlarge view of XRD of ZO, SZO, CSZO-1, CSZO-2, CSZO-3 nanomaterials.

Table 2 Crystallite size, micro strain, and dislocation density values of the catalysts

Samples	Debye–Scherrer method			Williamson–Hall method		
	Crystallite size (nm)	Microstrain (ε) $\times 10^{-3}$	Dislocation density (δ) $\times 10^{-3}$	Crystallite size (nm)	Microstrain (ε) $\times 10^{-3}$	Dislocation density (δ) $\times 10^{-3}$
ZO	38.98	2.31	0.93	37.88	0.17	0.70
SZO	29.97	3.84	1.49	38.51	0.94	0.68
CSZO-1	46.02	2.66	0.63	51.16	0.42	0.38
CSZO-2	35.85	5.80	1.46	60.81	0.11	0.27
CSZO-3	35.74	3.02	1.04	43.32	0.70	0.53

$$\delta = \frac{1}{D^2} \quad (4)$$

An increase in dislocation density and microstrain has been observed on doping and co-doping, which indicates distortion in the ZO lattice. This distortion may reduce nucleation and subsequent growth rates, ultimately leading to a decrease in the crystallite size of the synthesized nanomaterials. Debye–Scherrer method neglects the contribution of lattice strain to peak broadening, the Williamson–Hall (W–H) method (Fig. 2), based on uniform deformation model was employed to separate size and strain-induced broadening effects using eqn (5).[39]

$$\beta \cos\theta = \frac{K\lambda}{D_{W-H}} + 4\varepsilon \sin\theta \quad (5)$$

A linear plot of $\beta \cos\theta$ *versus* $4 \sin\theta$, yields the microstrain from the slop and the crystallite size from the intercept.[24] As summarize in Table 2, the crystallite size obtained from the W–H method are generally larger than those estimated by Scherrer equation, reflecting the removal of strain-induced broadening effects. The SZO exhibit higher microstrain, consistent with lattice distortion caused by Sr^{2+} substitution, where as the Cu/Sr co-doped samples show comparatively lower microstrain values, indicating partial strain relaxation and improved crystalline ordering.

FTIR analysis was performed to analyse the bond vibrations and functional groups present in the synthesized samples. Fig. 3a depicts the FTIR spectra of ZO, SZO, CSZO-1, CSZO-2, and CSZO-3, obtained over the wavelength range of 400–4000 cm^{-1}. An intense peak originating at 400 cm^{-1} in ZO spectrum corresponds to Zn–O bond stretching vibration, which is commonly observed in ZnO-based nanomaterials.[40] On the other hand, a band between 403 and 580 cm^{-1} also verifies the Zn–O–Zn vibrational mode at the surface of the wurtzite ZO lattice and confirms the synthesis of ZO nanomaterial. A band at 1107 cm^{-1} in the SZO spectrum can be attributed to the Sr–O–Sr stretching vibrations.[41] The band at 1457 cm^{-1} corresponds

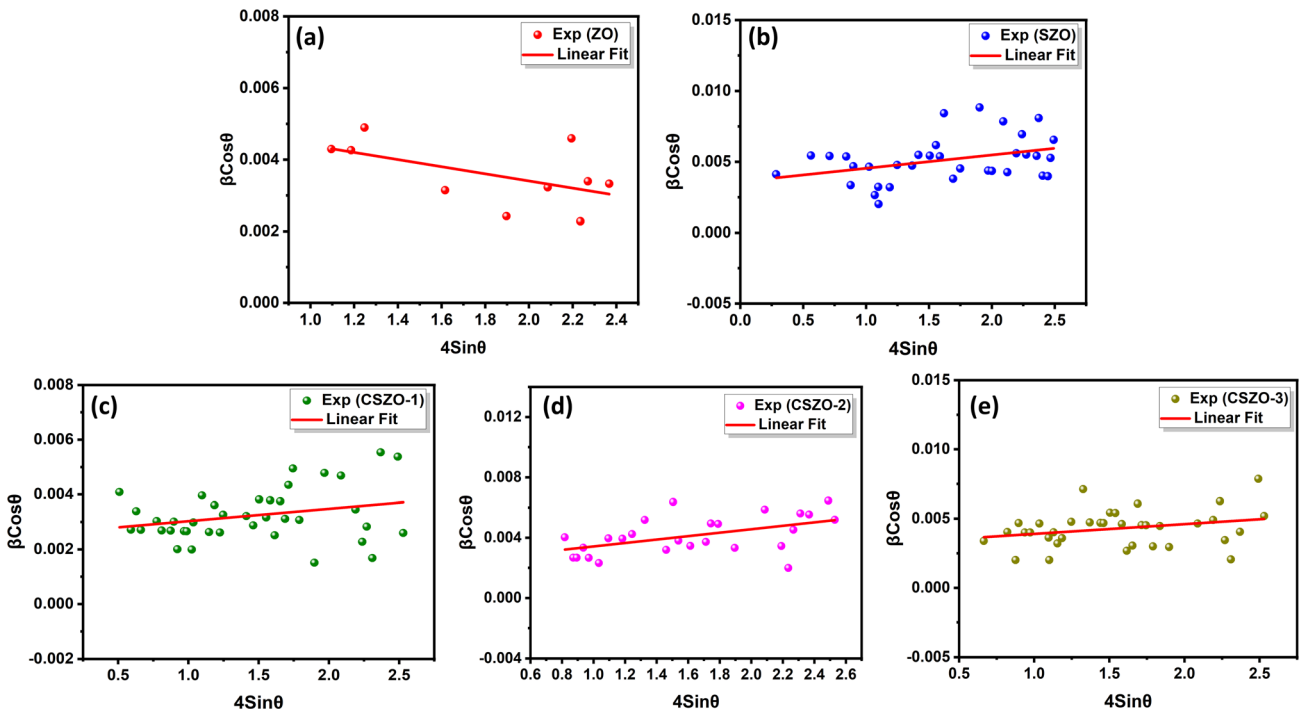

Fig. 2 Williamson–Hall plot of (a) ZO, (b) SZO, (c) CSZO-1, (d) CSZO-2, (e) CSZO-3.

to the C=O of adsorbed CO_2 at the surface of the samples.[42] A band observed at 3310 to 3617 cm^{-1} arises due to O–H stretching vibrations of adsorbed water molecules on the catalyst surface,[43,44] while a peak at 1648 cm^{-1} is due to the bending vibration of the H–O–H group in the water molecule present at the surfaces of all synthesized materials, which has also been reported in literature.[45] Further, a peak detected at 2334 cm^{-1} may be due to asymmetric stretching of the C=O bond. Peaks in the range of 611–730 cm^{-1} in CSZO-1, CSZO-2, and CSZO-3 may correspond to metal oxygen (M–O) (M = Cu, Sr) stretching vibrations.[46,47] However, changes in peak intensities and a slight shift in peak positions have also been observed in doped and co-doped samples.

The chemical states of the host elements (Zn, O) and dopants (Sr, Cu) in the CSZO-2 photocatalyst were investigated by XPS analysis. The survey spectrum of CSZO-2 photocatalyst (Fig. 3b) confirms the presence of Zn $2p_{1/2}$, Zn $2p_{3/2}$, O1s, Sr $3d_{3/2}$, Sr $3d_{5/2}$, and Cu 2p. Surface charging during XPS measurements was compensated using the instrument's charge neutralization system, and binding energies were calibrated accordingly. Peak deconvolution was performed using mixed Gaussian–Lorentzian function, and standard constraints on spin–orbit splitting, area ratios and full width at half maximum (FWHM) were applied for all core-level doublets.

The narrow scan XPS spectra of Zn 2p core level show two peaks of $2p_{3/2}$ and $2p_{1/2}$ at 1025.8 and 1048.9 eV, respectively, as shown in Fig. 3c. The energy separation between these two peaks is 23.1 eV, which suggests that Zn in CSZO-2 exists in the +2 oxidation state.[48] Fig. 3d shows XPS data of O 1s for the CSZO-2, and three distinct energy peaks at low, middle, and high binding energies at 530.1, 530.9, and 531.9 eV can be seen. The low binding energy peak at 530.1 eV can be attributed to O^{2-} in Zn–O bond in ZO lattice, while the middle binding energy peak at 530.9 eV is associated with O^{2-} as oxygen vacancy in ZO lattice. The high binding energy peak at 531.9 eV corresponds to C=O or H_2O at the surface of the photocatalyst.[49] The presence of oxygen vacancies plays a important role in charge separation and photocatalytic activity.

Fig. 3e shows Sr 3d spectrum, which exhibit a spin-orbit doublet with binding energies at 133.8 eV and 138 eV that are associated with Sr $3d_{5/2}$ and Sr $3d_{2/3}$, respectively. The absence of additional Sr-related spectral features suggests that Sr is predominantly incorporated into the ZO lattice. Given the low dopant concentration, Sr^{2+} is inferred to substitute Zn^{2+} sites in the ZO lattice, causing lattice distortion, which is in agreement with the observed XRD peak shifts.[50] Fig. 3f shows the high-resolution XPS spectrum of Cu 2p core level, where spin–orbit doublet at 933.6 (Cu $2p_{3/2}$) and 953.7 eV (Cu $2p_{1/2}$) can be seen, separated by 20.1 eV, which suggests that Cu is co-doped in ZO as Cu^{2+}.[51] In addition, weak shake-up satellite features are observed at higher binding energies, further supporting this assignment. No distinct spectral features corresponding to Cu^{+} or metallic Cu are observed, indicating that Cu in predominantly present as Cu^{2+} and is highly dispersed within the ZO matrix.

3.2 Morphological analysis

In order to analyse the surface morphology of the synthesized doped and undoped nanomaterials, SEM analysis was

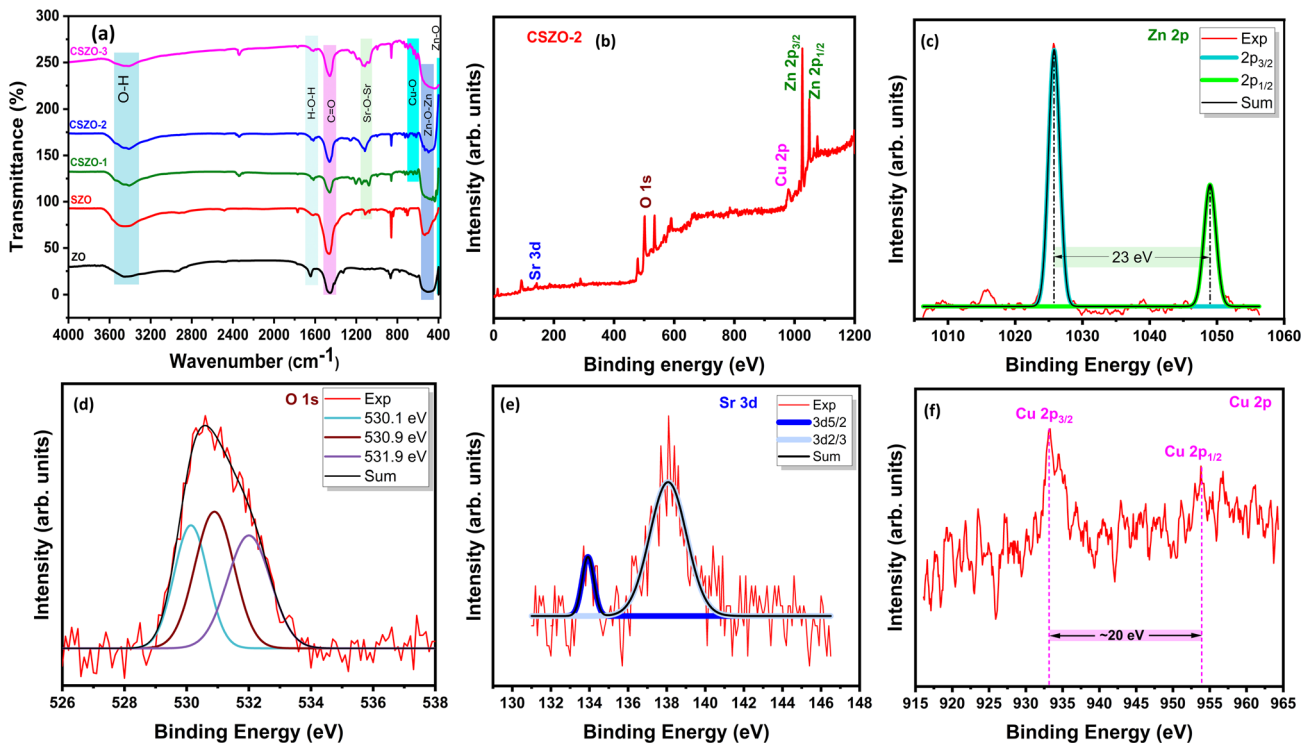

Fig. 3 (a) FTIR spectra and (b) XPS survey spectrum and high-resolution spectra of (c) Zn 2p, (d) O 1s (e) Sr 3d (f) Cu 2p of CSZO-2 catalyst.

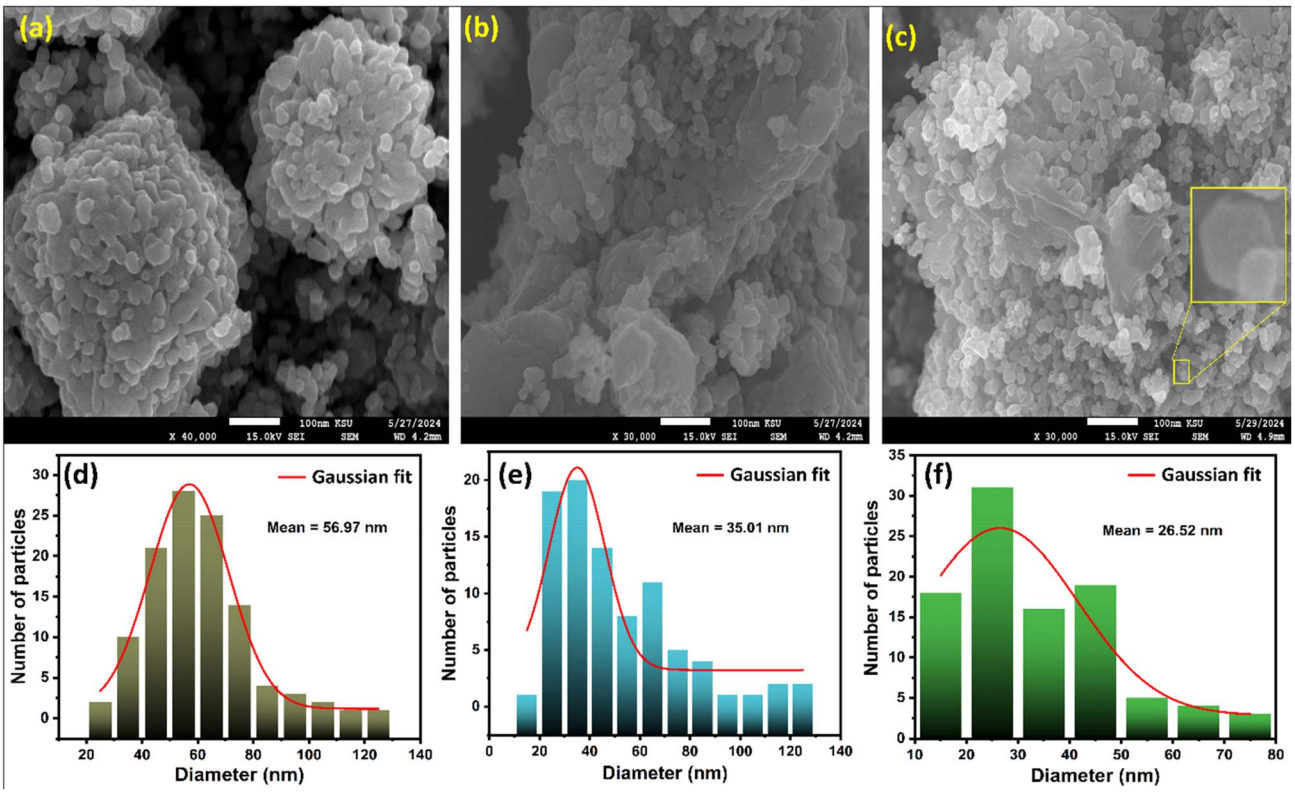

Fig. 4 SEM images of (a) ZO, (b) SZO (c) CSZO-2 nanomaterials, and (d–f) the corresponding diameter distribution histogram plots.

performed. SEM micrographs of ZO, SZO, and CSZO-2 photocatalysts recorded at the same magnification (scale bar 100 nm) are depicted in Fig. 4(a–c). The pristine ZO sample exhibits densely packed nanograins with irregular morphology and noticeable agglomeration, with a particle size in the range of 15–80 nm. Upon doping and co-doping of Sr^{2+} and Cu^{2+} (Fig. 4c), the morphology shows a reduction in particle size (10–40 nm) along with comparatively less compact agglomeration, suggesting that doping suppresses the grain growth during synthesis. After doping and co-doping, a decrease in particle size is observed, while the hexagonal disk-shaped structure of the nanomaterial remains intact, which is aligns with earlier reported findings.[52] Quantitative particle size analysis was conducted using ImageJ software, by measuring more than 100 particles for each sample, and corresponding size distribution histograms are shown in Fig. 4(d–f). Gaussian fitting of size distribution yielded an average particle size of 56.97 nm, 35.01 nm, and 26.52 nm for ZO, SZO, and CSZO-2, respectively. Incorporation of Cu^{2+} and Sr^{2+} into the ZO decreased the particle size, and confirm the role of dopants in hindering crystallite growth, which is consistent with the peak broadening observation in XRD analysis. Although a decrease in the particle size is generally associated with an increase in surface to volume ratio, which ultimately increases the surface area. The large surface area of CSZO-2 increases the exposure of active sites, improve reaction kinetics, and enhances its catalytic performance. The observed surface roughness and grain structure of CSZO-2 indicate high potential for photocatalytic activity. Some aggregation in the CSZO-2 is also observed, which is due to high surface energy caused by the dopant incorporation, facilitating the adsorption of organic pollutants and improve light interaction.

The morphology and structure of ZO, SZO, and CSZO-2 nanoparticles were further analysed by using TEM. Fig. 5(a–c) reveals nanomaterials with predominantly quasi-spherical, and irregular morphologies, which tend to form aggregate due to their high surface energy and strong van der Waals interactions at the nanoscale.[53] The average particle size of as-synthesized ZO, SZO, and CSZO-2 photocatalysts were approximately 53.42 nm, 32.23 nm, and 25.15 nm, respectively, as shown in Fig. 5(d–f). These TEM results validate the morphological features observed in SEM and indicate reduction in particle size upon co-doping.

3.3 Surface area analysis

The textural properties of all the synthesized samples (ZO, SZO, CSZO-1, CSZO-2, and CSZO-3) were investigated by Brunauer–Emmett–Teller (BET) and Barrett–Joyner–Halenda (BJH) methods and the corresponding surface area, pore volume, and pore size values are summarized in Table 3. Fig. 6(a–e) presents the adsorption–desorption isotherms recorded at 77 k. All samples exhibit type IV isotherms with pronounced H3 hysteresis loops, which indicate that synthesized materials are mesoporous (pore size 2–50 nm). The sharp increase in adsorption at higher relative pressures ($P/P_0 > 0.8$), is indicative of capillary condensation process occurring within interparticle spaces.[54] The presence of H3-type hysteresis loops suggests slit-shaped pores originating from the aggregation of plate-like

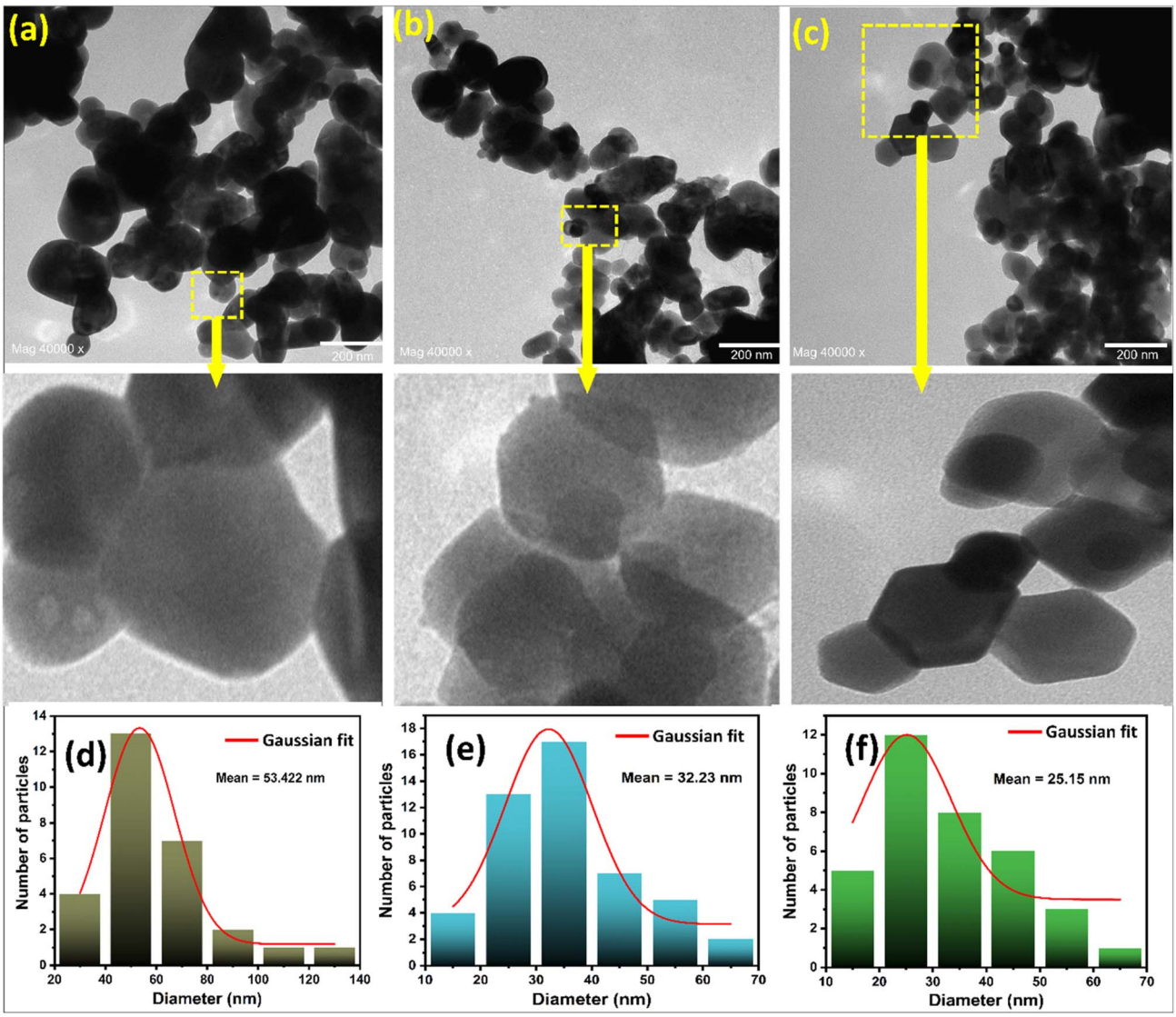

Fig. 5 TEM images of (a) ZO, (b) SZO (c) CSZO-2 nanomaterials, and (d–f) the corresponding diameter distribution histogram plots.

Table 3 BET surface area, pore volume, and pore Size of synthesized samples

Sample code	BET surface area (m^2 g^{-1})	Pore volume (cm^3 g^{-1})	Pore size (nm)
ZO	10.16	0.121	46.07
SZO	10.61	0.157	42.28
CSZO-1	14.85	0.072	34.82
CSZO-2	18.02	0.320	28.55
CSZO-3	17.63	0.097	31.98

particles, where porosity is primarily governed by interparticle voids rather than well-defined cylindrical pores.

The BET specific surface area of ZO was recorded as 10.16 m^2 g^{-1}, which increased slightly to 10.61 m^2 g^{-1} upon Sr^{2+} doping, (SZO), accompanied by a modest reduction in the average pore size. However, co-doping with Cu^{2+} led to noticeable changes in the textural parameters. CSZO-1 exhibited a moderate increase in surface area (14.85 m^2 g^{-1}) with reduced pore volume. Whereas CSZO-2 showed the highest surface area (18.02 m^2 g^{-1}), with smaller pore size (28.55 nm) and reduced pore volume, 0.041 cm^3 g^{-1}. These changes may be associated with improved dispersion of Cu ions within the ZO matrix, leading to reduced particle agglomeration and formation of a mesoporous network dominated by accessible interparticle voids. Although CSZO-3 retained a relatively high surface area, a decrease in pore volume was observed, likely due to denser particle packing at higher dopant content.[22] These findings highlight the critical role of co-doping in altering the porosity of the nanomaterial, particle aggregation and interparticle spacing, which provided more binding sites for dye molecules to adsorb, and ultimately enhancing the photocatalytic activity.[55]

3.4 Optical analysis

Optical properties of the synthesized samples (ZO, SZO, CSZO-1, CSZO-2, and CSZO-3) were examined using a UV-vis

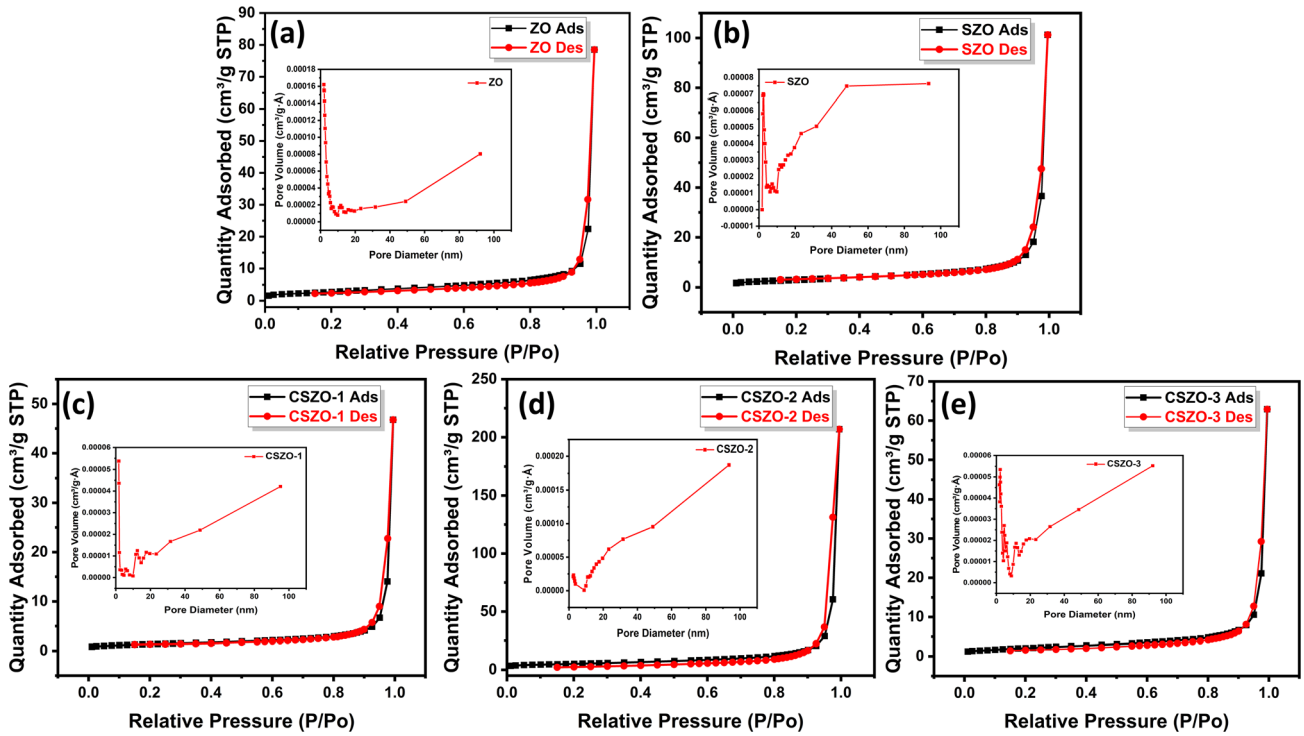

Fig. 6 N_2 adsorption desorption isotherm (a) ZO, (b) SZO (c) CSZO-1, (d) CSZO-2 (e) CSZO-3 nanomaterials (inset: BJH pore size distribution).

spectrophotometer in the range of 200–800 nm. The UV-vis absorption spectra of all photocatalysts are presented in Fig. 7a. The absorption edge of ZO was observed at 370 nm, which suggests negligible absorption in the visible-light region.

The photocatalyst underwent a red shift to the visible region when Sr^{2+} and Cu^{2+} were incorporated into the ZnO matrix. This shift toward higher wavelengths is because of the combined effect of the dopants in changing the local structure of ZO.[56] In particular, Cu^{2+} incorporation introduces localized Cu 3d states

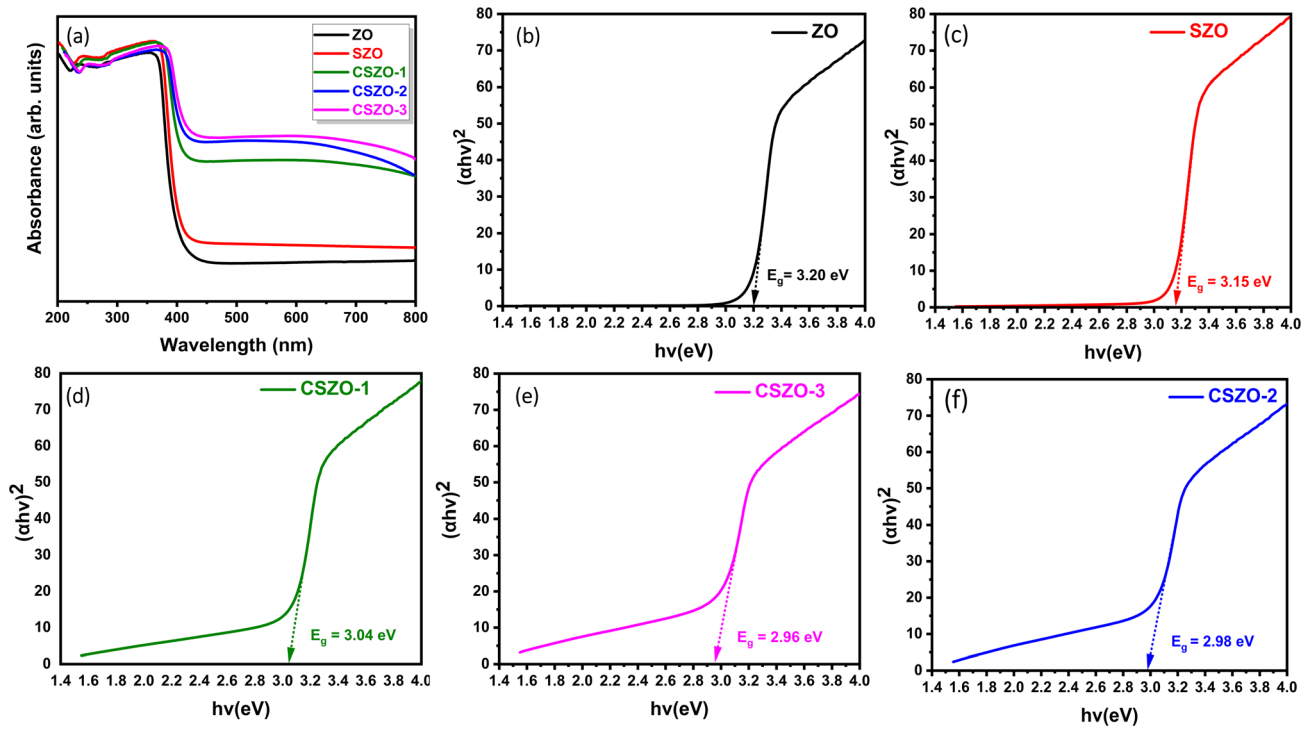

Fig. 7 (a) UV-visible absorption spectra and Tauc plot of (b) ZO, (c) SZO (d) CSZO-1, (e) CSZO-2 (f) CSZO-3 nanomaterials.

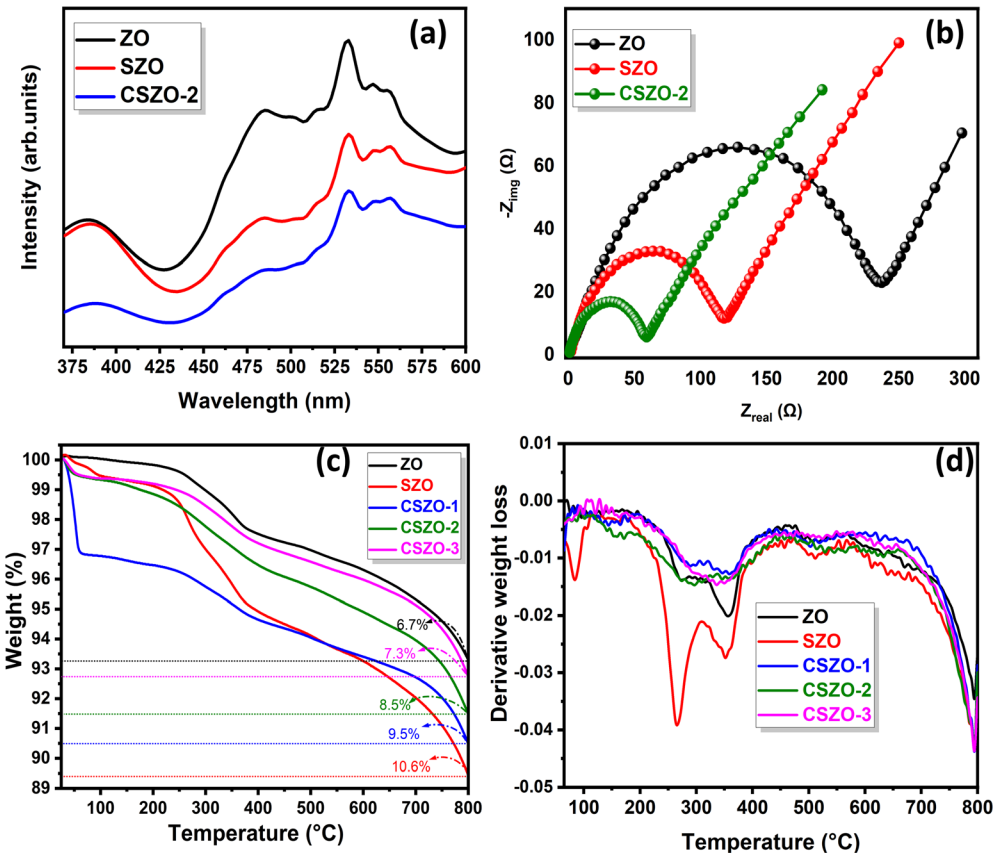

Fig. 8 (a) PL (b) EIS Nyquist plots of ZO, SZO, and CSZO-2 (c) TGA (d) DTG curves of ZO, SZO, CSZO-1, CSZO-2, CSZO-3 nanomaterials.

within the band gap, while Sr^{2+} substitution induces lattice distortion and polarization effects due to ionic size mismatch. The combined effect of these dopants results in enhanced band tail formation in the co-doped samples. The Tauc's eqn (6) was used to calculate the optical band gap (E_g) of the synthesized samples.[57]

$$(\alpha h\nu)^n = A(h\nu - E_g) \quad (6)$$

where α corresponds to the absorption coefficient, h is Planck's constant, ν is the frequency of incident light, A is the proportionality constant and $n = 2$ corresponds to allowed direct electronic transitions. ZnO is a well-established direct band gap semiconductor, therefore plots of $(\alpha h\nu)^2$ *vs.* $h\nu$ were employed to determine the optical band-gap. Although dopant incorporation may introduce localized states within band-gap, the dominant optical transition in the doped ZnO systems remains direct, as widely reported in the literature.[58–60] The band gap energies were obtained by extrapolating the linear portion of the high absorption region near the absorption edge to the photon energy, while excluding low-energy absorption tails associated with defect related states. The estimated band gaps for ZO, doped SZO, and co-doped CSZO-1, CSZO-2, and CSZO-3 are 3.20 eV, 3.15 eV, 3.04 eV, 2.98 eV, and 2.96 eV, respectively, as illustrated in Fig. 7(b–f). The incorporation of dopants in the ZO lattice leads to a pronounced reduction in its band gap. This progressive reduction in band gap can be attributed to dopant-induced localized defect-related states, lattice distortion, and changes in electronic band structure.[20]

Photoluminescence (PL) spectroscopy was also employed to investigate the optical and defect-related emission behaviour of pure and co-doped samples. This technique offers valuable information regarding charge-carrier recombination, band structure and defect states, which are essential for understanding the optical and electrical behaviour of synthesized samples.[61] The PL spectra of undoped, Sr-doped and Cu/Sr co-doped ZnO samples were recorded at 392 nm excitation and are shown in Fig. 8a. Since PL emission mainly originates from the radiative recombination of e^- and h^+, its intensity is strongly correlated with charge-carriers recombination kinetics and consequently, photocatalytic performance. In general, a higher PL intensity implies faster recombination of e^- and h^+, whereas PL quenching indicates effective charge separation and prolonged carrier lifetime.[62] The PL spectrum of undoped, doped and co-doped samples exhibit a peak centered at 386 nm which corresponds to near band-edge (NBE) emission and is attributed to interband recombination of e^- and h^+. In addition, multiple emission bands in 480–555 nm range arises from radiative recombination involving intrinsic defects states such as zinc interstitials (Zn_i), oxygen vacancies (V_o) and zinc vacancies (V_{Zn}). In particular the green emission at 532 nm is commonly attributed to oxygen vacancies (V_o), acting as deep-level defects in ZO band gap, and zinc interstitials (Zn_i) related transitions.[34] The orange-red emission near 608 nm

originates from deep-level or surface-related defects states. Compared with ZO, SZO exhibits a marked reduction in PL intensity, over the entire visible region, indicating suppression of e^- and h^+ recombination. Suggesting that Sr doping modifies the defect landscape and introduces localized states that promote more efficient charge separation.[63] A more pronounced PL quenching is observed in CSZO-2 samples, demonstrating the most effective inhibition of charge carrier recombination. The incorporation of Cu ions introduce additional localized energy levels within the ZO band structure, and further modify the recombination pathways.[64] The synergistic effect of Cu and Sr codoping promotes defect-assisted charge separation and carrier trapping, resulting in significantly reduced PL intensity, including suppression of deep-level emissions. Overall, the progressive decrease in PL intensity from ZO to CSZO-2 confirms the enhanced charge and reduced recombination of photogenerated charge carriers in the co-doped system which is highly beneficial for photocatalytic application.

3.5 Electrochemical and thermal analysis

The electrochemical impedance spectroscopy (EIS) was carried out to evaluate the impact of co-doping on charge transfer dynamics in the synthesized nanomaterials. The EIS measurements were performed using 1 M KOH solution with a frequency range of 0.01−100 kHz and the resulting Nyquist plots are presented in Fig. 8b. Each plot exhibits two characteristic parts, a semicircle in the high-frequency region followed by a linear part in the low-frequency region. The offset of the high frequency intercept from the origin on the real impedance axis (Z_{real}) represents the solution resistance (R_s) of the electrolyte. The R_s values for the prepared samples ZO, SZO and CSZO-2 are 1.7 Ω, 1.3 Ω, and 0.99 Ω. The diameter of the semicircular arc corresponds to the charge transfer resistance (R_{ct}) of the materials coated on the electrode.[65] A larger arc radius denotes higher R_{ct} and smaller radius reflects lower R_{ct}. The R_{ct} values for ZO, SZO and CSZO-2 are 235 Ω 117 Ω and 58 Ω. As CSZO-2 exhibits the smallest R_{ct} value compared with both pristine ZO and doped SZO, indicating lower charge transfer resistance. The reduced R_{ct} effectively improves the electrochemical properties of the co-doped material, leading to improved photocatalytic activity by suppressing the recombination of photogenerated e^-/h^+ pairs. The inclined line appearing in the low-frequency region is associated with Warburg impedance (Z_w), which arises from ion diffusion and concentration polarization effects during the electrochemical process.

Thermal analysis of the ZO, SZO, CSZO-1, CSZO-2, and CSZO-3 samples was conducted to evaluate their thermal stability and mass changes using TGA and its first derivative (DTG), from ambient temperature to 800 °C. As shown in Fig. 8(c and d) both the TGA curves and corresponding DTG profiles reveal three regions of mass loss. All samples exhibit a minor weight loss of approximately 0.5% below 100 °C, except CSZO-1, which shows a significantly higher weight loss of 3.2% in this region. This initial weight loss is associated with the desorption of physically bound water molecules from the catalysts surface.[66] Correspondingly, the DTG curves show a low-temperature peak centered around 70–80 °C, with CSZO-1 showing a noticeably higher intensity peak, indicating a higher rate of moisture desorption. In the second region, a weight loss of 5.6% occurs from 200 to 450 °C, which is likely due to the removal of chemically bound water and the thermal decomposition of organic contents.[67,68] This decomposition process is clearly reflected in the DTG minima, indicating maximum decomposition rate around 300–350 °C. Finally, between 450 and 800 °C, an additional 1–5% weight loss was recorded for different samples, which indicates the formation of themally stable nanomaterials after complete decomposition of precursors.[69] This stage is represented in the DTG profiles as broad, low intensity peaks, signifying a slow and continuous mass loss process.

However, ZO exhibits the lowest overall weight loss of 6.7%, while that of doped SZO shows the highest weight loss among all samples (approximately 10.6%), indicating reduced thermal stability upon single dopant incorporation. In contrast, the co-doped CSZO-1, CSZO-2, and CSZO-3 samples demonstrate progressively improved thermal stability with increasing Cu content, as evident by 9.5% weight loss for CSZO-1 to 7.3% for CSZO-3. This trend is further supported by the DTG data, where the main decomposition peaks of co-doped samples shift slightly to higher temperatures and exhibit reduced intensity compared to SZO, indicating delayed decomposition and enhanced thermal stability. A slightly higher weight loss in single doped materials indicates dopant induced lattice modification, which initially destabilized the ZO framework; however, co-doping compensates this effect and restored thermal stability.[70] In addition to total mass loss, the residual mass at 800 °C provides further insight into the thermal robustness of the samples. The co-doped materials exhibit higher residual mass compared to SZO, indicating a more stable inorganic oxide framework after complete precursor decomposition. This enhanced residue retention suggests stronger metal–oxygen bonding and improved lattice integrity induced by Cu–Sr codoping, which effectively suppresses thermally driven structural degradation and supports the enhanced functional stability of the co-doped photocatalysts.

4 Assessment of photocatalytic efficiency

The photocatalytic potential of the prepared catalysts ZO, SZO, CSZO-1, CSZO-2, and CSZO-3 for environmental remediation was explored by investigating the degradation of CR, used as a model organic pollutant, under visible-light irradiation. Prior to illumination, the catalyst-dye suspensions were magnetically stirred in the dark to establish adsorption–desorption equilibrium between CR molecules and the catalyst surface. The UV-vis absorption spectra showing the temporal evolution of CR degradation over ZO, SZO, and CSZO-2, with maximum absorption peak at 500 nm are shown in Fig. 9a–c. Upon exposure to visible-light in the presence of as-prepared catalysts, a significant decrease in the absorbance intensity of CR

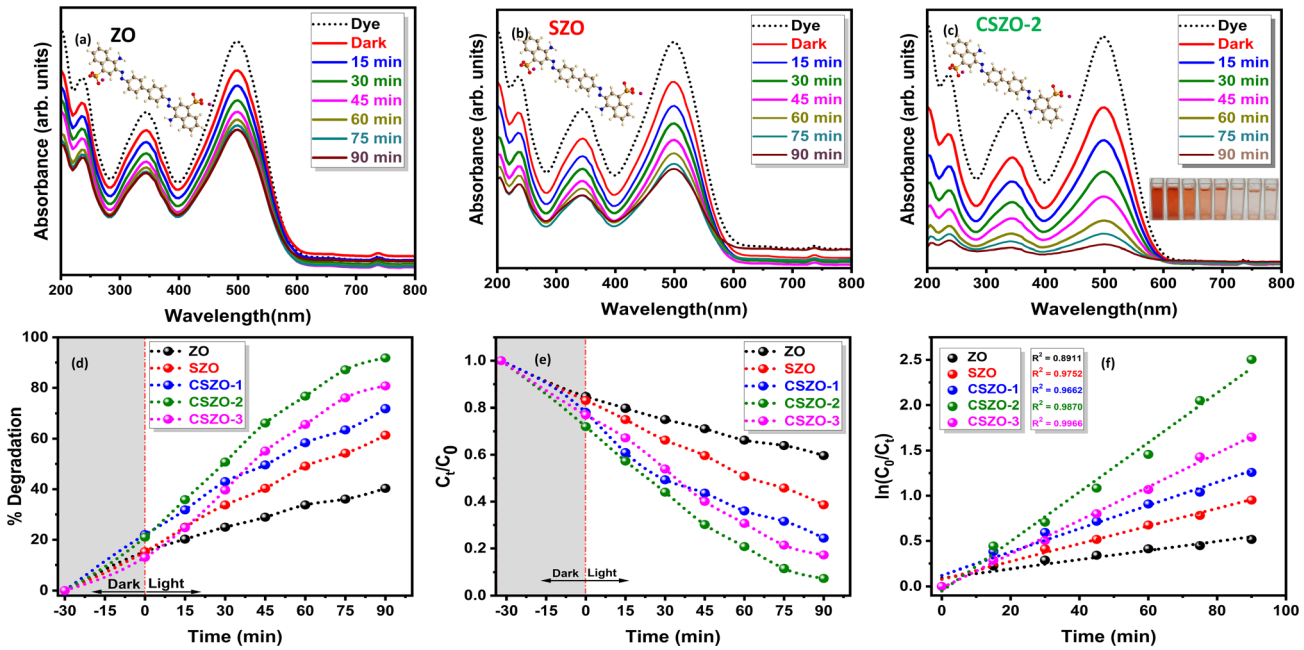

Fig. 9 UV-vis spectra of CR using (a) ZO, (b) SZO, (c) CSZO-2 and (d) % degradation (e) kinetic plots of C_t/C_0 (f) linear fitting plots of CR degradation using ZO, SZO, CSZO-1, CSZO-2, CSZO-3 nanomaterials.

dye is recorded. The CSZO-2 catalyst exhibited the highest degradation efficiency of 91.82%, while ZO, SZO, CSZO-1 and CSZO-3 showed 40.34%, 61.38%, 71.79%, and 80.73% degradation efficiency, respectively as shown in Fig. 9d. The codoped CSZO-2 catalyst exhibit enhance photocatalytic activity due to its superior light absorption capacity compared to other samples.

The temporal decrease in CR concentration with irradiation time (Fig. 9e) follows the order CSZO-2 > CSZO-3 > CSZO-1 > SZO > ZO, demonstrating a progressive improvement in the photocatalytic degradation of CR. The kinetics of CR degradation were estimated using eqn (7);

$$\ln\frac{C_0}{C_t} = kt \tag{7}$$

Here, C_0, C_t, and k represent the CR concentration before irradatition, concentration of dye at irradiation time t, and rate constant. The plots of $\ln(C_o/C_t)$ *versus* time (Fig. 9f) exhibit linearity, confirming that the degradation process follows pseudo-first-order kinetics under applied experimental conditions. The regression coefficients (R^2) were found to be 0.8911, 0.9752, 0.9662, 0.9870 and 0.9966 for ZO, SZO, CSZO-1, CSZO-2, and CSZO-3, respectively. The corresponding rate constants were calculated to be 0.005 min^{-1}, 0.010 min^{-1}, 0.013 min^{-1}, 0.028 min^{-1}, and 0.019 min^{-1}. Notably, CSZO-2 exhibited the highest rate constant for CR degradation, showing its superior photocatalytic efficiency compared with other synthesized catalysts. This improvement in the photocatalytic performance of CSZO-2 can be attributed to the more efficient generation and separation of photoinduced charge carriers under visible-light irradiation, as supported by PL and EIS analysis. However, excessive Cu incorporation (as in CSZO-3) results in reduced activity, which may be associated with agglomeration and partial blockage of active sites, thereby limiting interfacial electron transfer.

4.1 Effect of CSZO-2 dose

The effect of CSZO-2 catalyst dosage on the photodegradation of CR dye was studied by increasing catalyst mass from 5 to 20 mg while keeping other parameters constant. Fig. 10a demonstrates the UV-vis absorbance spectra of the dye, clearly showing a decrease in absorbance intensity with increasing irradiation time, indicating dye degradation. Increasing the catalyst amount from 5 to 15 mg enhanced the CR degradation from 64% to 97.42% (Fig. 10b) owing to increased availability of surface active sites, and enhanced generation of reactive species such as $\cdot O^{2-}$ and $\cdot OH$ radicals. However, further increase in the catalyst dose (20 mg) resulted in a decline in the photocatalytic activity. This can be attributed to increaased solution turbidity, photon scattering, impaired light transmission through the reaction medium at higher catalyst concentration, which diminish photon absorption by active sites and induces saturation effects.[71] Consequently, 15 mg of CSZO-2 was identified as the optimal catalyst dose for CR degradation, as it provided maximum efficiency without adverse effects associated with higher dosage. Kinetic analysis (Fig. 10c and d) shows linear fitting and high R^2 values, confirming pseudo-first-order kinetics. The rate constants for 5, 10, 15, and 20 mg of CSZO-2 catalyst are 0.022 min^{-1}, 0.027 min^{-1}, 0.040 min^{-1}, and 0.033 min^{-1}, respectively. The highest rate constant of 0.040 min^{-1} is recorded for 15 mg of sample, indicating optimal catalyst loading for degradation. However, beyond this threshold, a decline in k was noted, which suggests that further

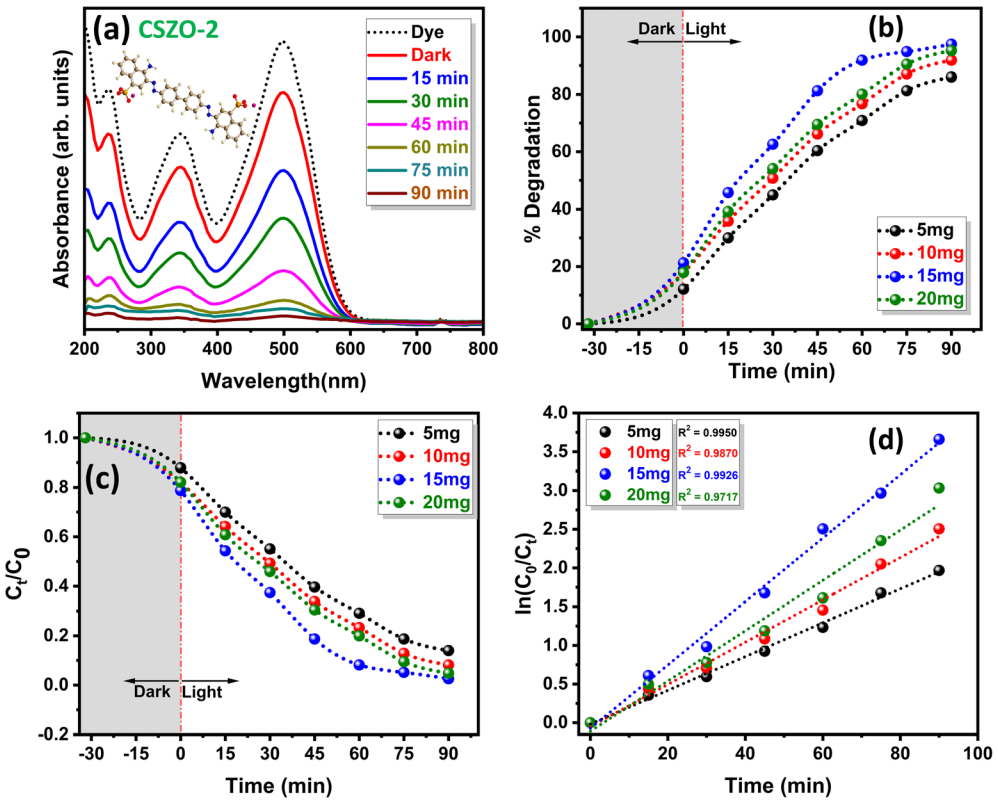

Fig. 10 (a) UV-vis spectra of CR (b) % degradation of CR (c) kinetic plots of C_t/C_0 *vs.* time and (d) linear fitting plots of CR degradation over various doses of CSZO-2.

increases in catalyst mass do not result in proportional improvement in degradation efficiency. This may be due to the aggregation of catalyst, which curtails reactive sites accessibility and impedes light absorption.

4.2 Effect of CR concentration

The impact of CR concentration on degradation efficiency was evaluated at four different concentrations (10, 20, 30, and 40 ppm) using CSZO-2 as the photocatalyst. Fig. 11a displays the time-dependent UV-vis absorption spectra of CR dye degradation, and a continuous decrease in the absorbance of the CR can be observed after different time intervals and finally reaching at 0.1 after 90 min. The degradation efficiency decreases with increasing CR concentration (Fig. 11b) because at higher CR concentration, dye molecules overcrowd the catalyst's limited active sites. This saturation impedes the generation of $\cdot O^{2-}$ and $\cdot OH$ radicals. Moreover, the CR molecules themselves absorb light and reduce its penetration to the catalyst surface and ultimately decreasing photocatalytic activity. Fig. 11c demonstrates an inverse correlation between dye concentration and degradation efficiency. Kinetics of the reaction at various CR concentrations were analysed and the linear correlation in the plotted data and higher R^2 values for each concentration (Fig. 11d) validates the alignment of the degradation process with pseudo-first-order kinetics, where higher concentrations result in a slower reaction rate. The rate constants calculated for 10, 20,30, and 40 ppm solutions were 0.027 min^{-1}, 0.025 min^{-1}, 0.021 min^{-1}, and 0.016 min^{-1}, respectively. Results show that lower CR concentration has a higher rate constant value, reflecting its rapid degradation efficiency. A significant decline in the rate constant can be observed with increasing dye concentration, and a 40 ppm solution exhibits the lowest value. This trend can be attributed to less availability of $\cdot OH$ radicals and catalyst active sites. Thus, these findings demonstrate that, at low initial concentration, the degradation efficiency is high, while at higher CR concentration, the degradation efficiency is low due to the limited availability of binding sites at the catalyst surface.

4.3 Effect of solution pH

The adsorption and photocatalytic degradation of CR are strongly influenced by the solution pH due to pH-dependent surface charge variation of the catalyst. Prior to light irradiation, the reaction suspension was magnetically stirred in the dark until adsorption–desorption equilibrium was established. Thereby minimizing the contribution of pH-driven dye adsorption during photocatalytic evaluation.

All the experiments were performed under controlled conditions (solution volume: 50 mL, catalyst dose: 10 mg, CR concentration: 10 ppm, contact time: 90 min) to evaluate the degradation efficiency across a pH range of 2–8. As shown in Fig. 12a, the degradation efficiency increased from 75% at pH 2 to a maximum of 91% at pH 6.6 followed by a decline to 69% at pH 8. This trend is primarily governed by electrostatic

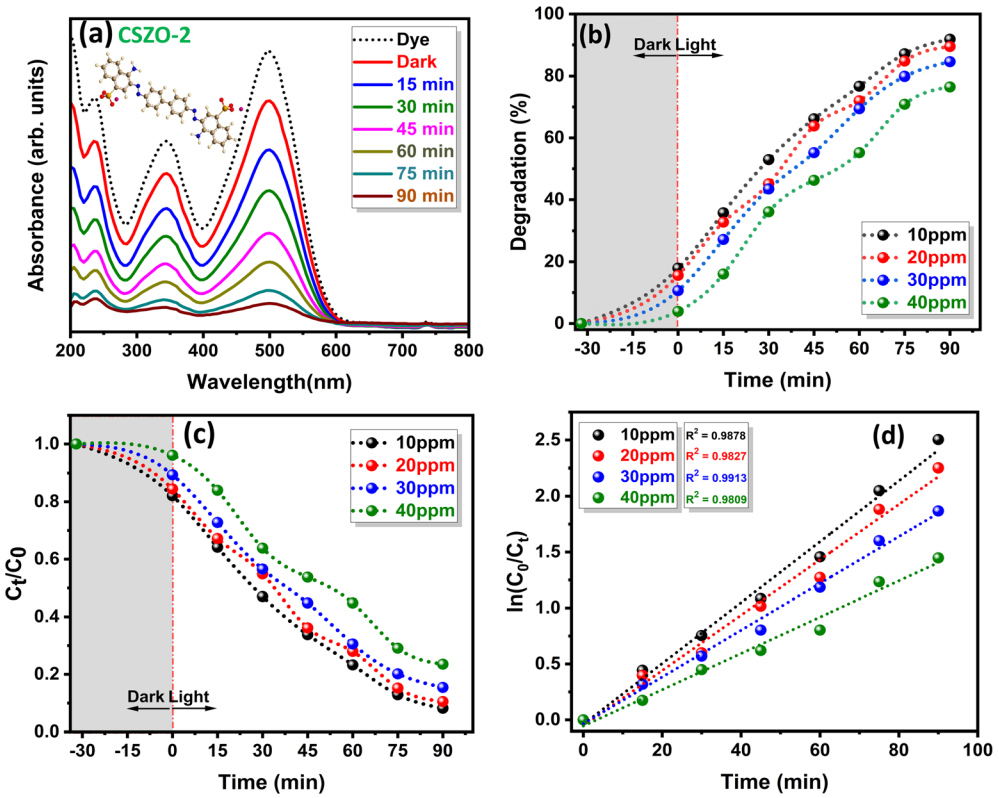

Fig. 11 (a) UV-vis spectra of CR using CSZO-2 (b) % degradation efficiency of CR (c) kinetic plots of C_t/C_0 *vs.* time (d) linear fitting plots of CR degradation at various concentration.

interactions among CR molecules and the catalyst surface. The point of zero change (pH_{PZC}) for CSZO-2 was determined *via* the salt addition method and recorded as 6.7. At lower pH (<6.7), the CSZO-2 surface becomes positively charged *via* protonation of –OH groups, favouring electrostatic interaction with negatively charged CR molecules. In addition, enhanced CR degradation under slightly acidic conditions (pH 6.6) can be attributed to the formation of ·OH radicals, at elevated pH, deprotonation of functional groups on the CSZO-2 surface occures, generating more OH groups that are key mediators in generating ·OH radicals.[72] However, at very low pH (pH 2) excessive CR adsorption onto the catalyst surface likely hinders light penetration and blocks active site, reducing catalytic activity.[73] Conversely, at higher pH (>6.7), hydroxyl groups on the CSZO-2 become negatively charged, creating electrostatic repulsion with anionic CR molecules, which hinders adsorption and ultimately reduces degradation efficiency.[74]

Fig. 12b shows the change in CR concentration with time at different pH values, while Fig. 12c shows the corresponding kinetic plots. After accounting for the dark adsorption–desorption equilibrium, the degradation data reasonably follow the pseudo first-order kinetic model. The calculated rate constants at pH 2, 4, 6.6, and 8 were 0.015 min^{-1}, 0.021 min^{-1}, 0.041 min^{-1}, 0.012 min^{-1} respectively. The high rate constant at pH 6.6, indicates faster photodegradation of CR dye.

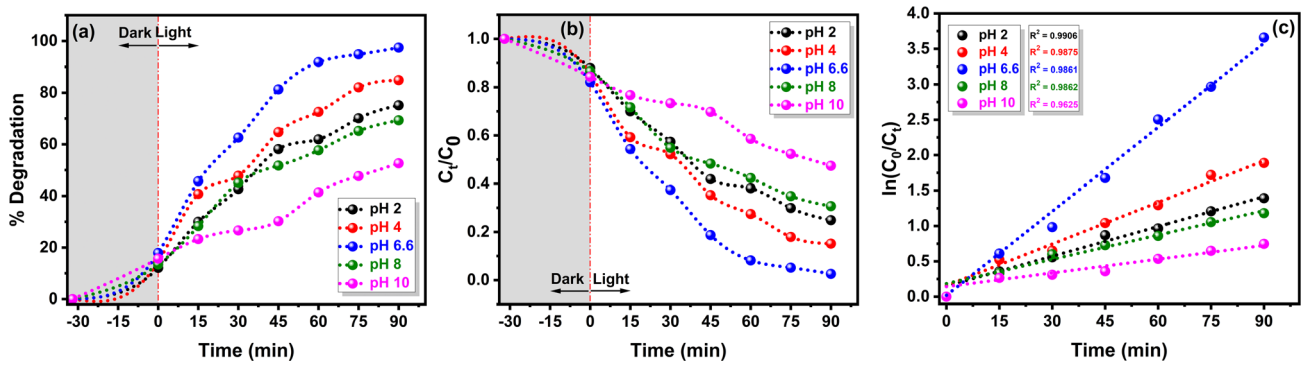

Fig. 12 (a) % degradation (b) kinetic plots of C_t/C_0 *vs.* time (c) linear fitting plots of CR degradation at different pH values using CSZO-2.

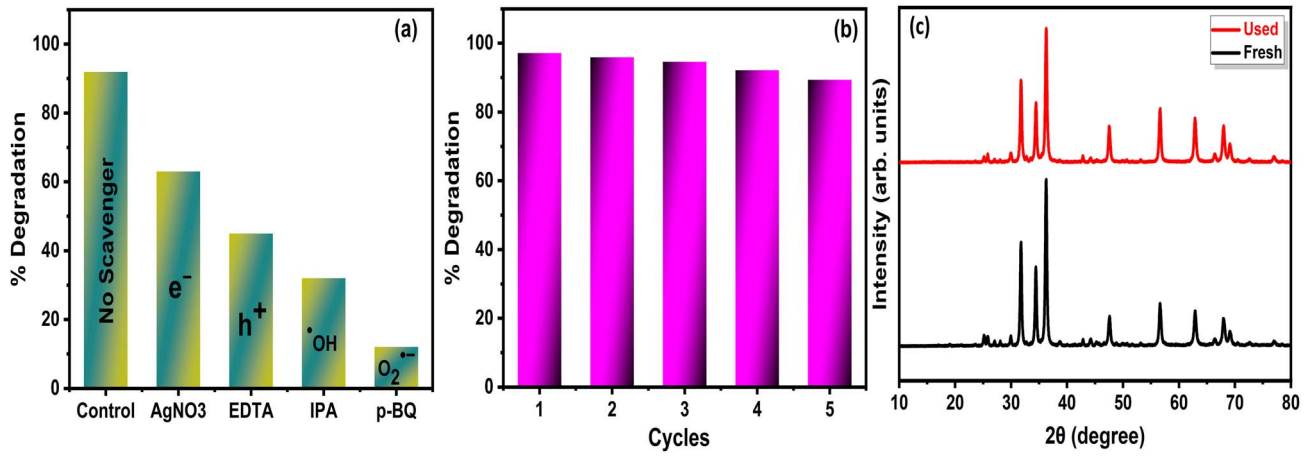

Fig. 13 (a) ROS capturing (b) recycle stability and (c) XRD patterns of fresh and used CSZO-2.

4.4 Scavenger study

To identify the key active species responsible for the photodegradation of CR, quenching experiments were conducted by introducing different radical scavengers into the reaction medium under identical experimental conditions as used in the assessment of the catalytic performance of the catalysts. Various scavengers such as EDTA, $AgNO_3$, IPA, *p*-BQ were employed for quenching h^+, e^-, ·OH and $O_2^{\cdot -}$ radicals respectively. As shown in Fig. 13a, the addition of $AgNO_3$ and EDTA caused only a marginal decrease in degradation efficiency, suggesting that the direct participation of e^- and h^+ in dye oxidation is limited under the present experimental conditions. In contrast, the addition of IPA and *p*-BQ resulted a decline in photocatalytic activity, indicating that ·OH and $O_2^{\cdot -}$ radicals are likely the predominant reactive species contributing to the degradation of CR dye.

4.5 Reusability and stability

The stability of the catalyst is of key importance for its practical application, and its reusability is an important indicator of its feasibility. To assess the stability of the CSZO-2 photocatalyst, reusability tests were conducted over five successive cycles under optimized conditions. Following each cycle, the catalyst was recovered and washed with DD water followed by ethanol, and then reused. Results demonstrate a 7.8% decline in the activity of the CSZO-2 catalyst after five repeated cycles, as

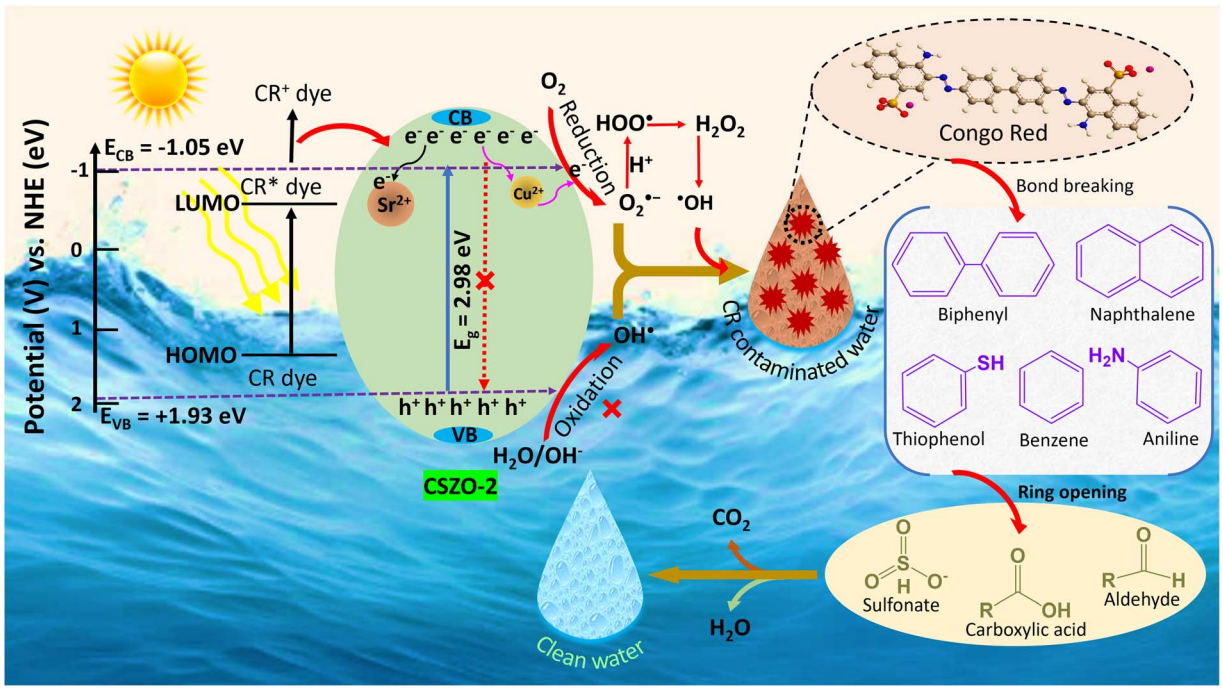

Fig. 14 Schematic representation of proposed mechanism of photocatalytic degradation of CR over CSZO-2 catalyst.

shown in Fig. 13b. This decrease in efficiency can be attributed to surface fouling, adsorption of by-products, and a reduction of active sites, possibly due to minor leaching of CSZO-2 catalyst during the recovery process.[75] Despite this slight reduction in photocatalytic efficiency over multiple cycles, the CSZO-2 catalyst retains significant activity, demonstrating effective reusability and positioning it as a promising candidate for photocatalytic applications. After photocatalytic experiment, the XRD patterns of the CSZO-2 were recorded (Fig. 13c) to evaluate the structural stability. All diffraction peaks remain at their original positions, indicating the structural stability of CSZO-2. A slight reduction in the peak intensity indicates a minor loss of crystallinity, which can be attributed to incomplete catalyst recovery or presence of residual impurities from the previous reaction cycles.[76]

4.6 Photodegradation mechanism

To gain a deeper understanding of the charge-transfer mechanism, the VB and CB band edge position of the CSZO-2 catalyst was estimated using the following eqn (8) and (9):

$$E_{VB} = \chi - E^{e} + 0.5\,E_{g} \quad (8)$$

$$E_{CB} = E_{VB} - E_{g} \quad (9)$$

Here, E_{VB} and E_{CB} denote valence band and conduction band potentials, respectively; χ is the absolute electronegativity, E_g and E^e represents the band gap energy and energy of free electrons (4.5 eV), respectively. Based on these calculations E_{VB} and E_{CB} edge position of CSZO-2 were estimated to be approximately +1.93 and −1.05 eV (*vs.* NHE), respectively. Fig. 14 illustrates the proposed photocatalytic mechanism of the CSZO-2 catalyst. The incorporation of Cu^{2+} and Sr^{2+} dopants is expected to induce defects levels and localized trapping sites, which can retard the recombination of photoinduced charge carriers and consequently accelerates the generation of radical species.[77] Upon exposure to visible-light, e^- are promoted from VB to the CB, leaving behind h^+ in the VB. These photogenerated e^- in the CB are captured by the dopant ions, which inhibit their recombination with the h^+ and facilitate the reduction of the molecular oxygen to $O_2^{\cdot -}$. These $O_2^{\cdot -}$ can further participate in a sequence of reactions to generate HOO· and ·OH. Both $O_2^{\cdot -}$ and ·OH are highly reactive species involved in the degradation of CR dye. Scavenger experiments indicate that $O_2^{\cdot -}$ and ·OH radicals play a dominant role in the CR degradation, while direct redox reaction by free h^+ and e^- remain comparatively limited. Nevertheless, photogenerated h^+ and e^- remain essential, as they initiate and sustain the formation of reactive oxygen species rather than directly degrading the dye molecules.[78] The overall photocatalytic degradation pathway of CR over CSZO-2 can be summarized as follows:

$$\text{CSZO-2} + h\nu \rightarrow \text{CSZO-2}(h_{VB}^{+} + e_{CB}^{-}) \quad (10)$$

$$\text{CSZO-2}(e_{CB}^{-}) + O_2 \rightarrow O_2^{\cdot -} \quad (11)$$

$$O_2^{\cdot -} + H^{+} \rightarrow HOO\cdot \quad (12)$$

$$2HOO\cdot \rightarrow H_2O_2 + O_2 \quad (13)$$

$$H_2O_2 + e^{-} \rightarrow OH^{-} + \cdot OH \quad (14)$$

$$O_2^{\cdot -}/\cdot OH + CR \rightarrow \text{degraded products } (H_2O + CO_2) \quad (15)$$

5 Conclusion

Cu/Sr co-doped ZnO nanomaterials were successfully synthesized *via* one-step chemical precipitation method and evaluated for the photocatalytic degradation of CR dye under visible-light. Structural analysis confirmed the retention of the wurtzite ZnO phase after Cu/Sr co-doping, with no significant structural distortion. XPS analysis verified the presence of Cu and Sr species in the ZnO lattice. UV-vis spectroscopy revealed a red shift in the absorption edge and a reduction in the band gap upon co-doping. PL spectra showed supressed emission intensity for the co-doped samples, indicating reduced charge-carrier recombination, while EIS measurements further supported the improved charge transfer behaviour of CSZO-2. Among all the synthesized samples, CSZO-2 exhibited highest photocatalytic activity, achieving approximately 97% degradation of CR within 90 min at natural pH, following pseudo first order kinetics. The scavengery study suggest that $O_2^{\cdot -}$ and ·OH were the main reactive species involved in the degradation process. The CSZO-2 catalyst, retaining 89% of its initial efficiency after five consecutive cycles, indicating good reusability and stability.

Conflicts of interest

There are no conflicts to declare.

Data availability

Data will be available on request.

Acknowledgements

This work was funded by Ongoing Research Funding program (ORF-2026-442), King Saud University, Riyadh, Saudi Arabia.

References

1 M. Kawsar, M. Sahadat Hossain, S. Tabassum, N. M. Bahadur and S. Ahmed, *RSC Adv.*, 2024, **14**, 11570–11583.
2 Y. C. Wei, H. E. Chang, P. Subramaniyan, S. C. Yu, Y. J. Hsu and T. E. Lin, *ACS Mater. Au*, 2025, **5**, 320–330.
3 B. Bhoi and V. Chandra, *ACS Sustainable Resour. Manage.*, 2025, **2**, 744–754.
4 A. S. Alawam, S. M. Mahgoub, A. A. Allam, A. M. Radalla, M. H. Shemy and R. Mahmoud, *RSC Adv.*, 2025, **15**, 43983–44006.
5 N. Ahmia, M. Benamira, L. Messaadia, R. Masmoudi, D. Horwat and I. Avramova, *J. Phys. Chem. Solids*, 2026, **208**, 113038.

6 R. Alabada, A. Ayub, Y. Ajaj, S. I. Bhat, R. H. Alshammari, A. Abduldayeva, A. I. Mallhi, Z. Ahmad and R. M. K. Mohamed, *J. Alloys Compd.*, 2024, **977**, 173400.
7 K. Abassi, A. Ben Ali, T. Ben Chaabane, M. Younas, C. M. Pecoraro, T. Altalhi, A. Mezni and M. Bellardita, *Mater. Chem. Phys.*, 2025, **344**, 131172.
8 A. Anitha, P. Ponmurugan, S. E. Natheer, S. Kannan, M. Sathishkumar and D. Arunkumar, *Mater. Sci. Eng., B*, 2025, **321**, 118478.
9 V. Q. Nguyen, M. A. Mahadadalkar, P. C. Nam, J. J. Shim, J. Singh, B. Van and D. D. Nguyen, *J. Taiwan Inst. Chem. Eng.*, 2025, **166**, 105520.
10 Jemini, S. Singh and B. Pal, *J. Taiwan Inst. Chem. Eng.*, 2025, **173**, 106151.
11 M. Pawar, P. Nain, S. Rani, B. Sharma, S. Kumar and M. A. Majeed Khan, *Opt. Mater.*, 2024, **157**, 116277.
12 G. Dhanasekaran, N. Parthiban, N. Nithya, D. Karthigaimuthu, G. Vijayakumar, S. Sangaraju and E. Thangavel, *Inorg. Chem. Commun.*, 2024, **170**, 113377.
13 M. Salmanizadeh and A. Sadeghzadeh-Attar, *J. Mol. Liq.*, 2024, **414**, 126271.
14 S. Pandey, S. K. Chauhan, A. Srivastava and R. K. Shukla, *Ceram. Int.*, 2025, **51**, 4929–4945.
15 Y. Zhu, D. Gao, J. Zeng, Z. Li, D. Li, D. Li, X. Hu, J. Lin, K. Liu, J. Wu and D. Wang, *Sep. Purif. Technol.*, 2026, **386**, 136561.
16 C. Wu, Z. Liu and J. Zhang, *J. Phys. Chem. Solids*, 2025, **207**, 112901.
17 A. Joy, M. R. Viswanathan, B. K. Vijayan, C. G. Silva, I. Basheer, S. Sugathan, P. A. Mohamed, A. Solaiappan and A. Shereef, *RSC Adv.*, 2024, **14**, 21655–21667.
18 K. Castelló Lux, J. Hot, V. Collière, M. L. Kahn, A. Bertron, E. Ringot, P. Fau and K. Fajerwerg, *J. Environ. Chem. Eng.*, 2025, **13**, 115110.
19 A. Mariappan, L. Harikrishnan, J. Eswaran, N. Arumugham, Y. Balasubramaniam, S. Daniel and R. Kanthapazham, *ACS Appl. Bio Mater.*, 2024, **7**, 2519–2532.
20 F. Khammar, S. Boukerche, S. Djaber, A. Boublia, A. Messabhia, A. Gharbi, H. Ferkous, C. V. Gomez, S. Bellucci, M. Albrahim, M. Alam and Y. Benguerba, *Inorg. Chem. Commun.*, 2025, **176**, 114274.
21 M. Arumugam, S. Acharya, H. Mohan, H. H. Yang, J. Venkatachalam and K. K. Seralathan, *Sep. Purif. Technol.*, 2025, **364**, 132522.
22 J. Khumphon, R. Ahmed, T. Imboon, J. Giri, N. Chattham, F. Mohammad, S. Kityakarn, V. Mangala Gowri and S. Thongmee, *ACS Omega*, 2025, **10**, 9337–9350.
23 H. Ahmad, A. B. Siddique, S. Zaheer, R. Sattar, A. Abbas, M. Amin, R. Al-Salahi, H. A. Abuelizz and M. Z. Saleem, *J. Water Process Eng.*, 2025, **74**, 107855.
24 P. Agale, V. Salve, S. Mardikar, S. Patange and P. More, *Appl. Surf. Sci.*, 2024, **672**, 160795.
25 A. Mudhoo, S. Paliya, P. Goswami, M. Singh, G. Lofrano, M. Carotenuto, F. Carraturo, G. Libralato, M. Guida, M. Usman and S. Kumar, *Environ. Chem. Lett.*, 2020, **18**, 1825–1903.
26 M. S. Hossain, S. M. Tuntun, N. M. Bahadur and S. Ahmed, *RSC Adv.*, 2022, **12**, 34080–34094.
27 A. K. Manna, S. N. Sarangi, J. Singh, N. N. K. Reddy, S. Varma and C. Yuvaraj, *Opt. Mater.*, 2026, **169**, 117624.
28 M. A. Rahman, M. T. Hossain, M. F. Ahmed, M. Shahriar Bashar, S. S. Dey, S. Ahmed and M. Sahadat Hossain, *Mater. Adv.*, 2025, **6**, 3686–3704.
29 C. E. Scanferla, C. A. Moreira, A. G. Oliveira, H. dos Santos, M. S. Gibin, F. Sato, R. R. S. de Farias, F. P. Garcia, C. V. Nakamura and D. M. F. de Oliveira, *Ceram. Int.*, 2025, **51**, 29303–29318.
30 A. G. Jerônimo, A. Lins, R. Barbosa, L. Neves, W. Albuquerque, P. Trigueiro, R. França, F. A. Huaman, F. P. Araujo and R. R. Peña-Garcia, *Mater. Res. Bull.*, 2026, **193**, 113704.
31 D. A. Sales, A. G. Jerônimo, P. Trigueiro, W. Albuquerque, R. Barbosa, L. Neves, L. C. Almeida, Y. Guerra, J. A. Osajima, E. Padrón-Hernández, B. C. Viana and R. R. Peña-Garcia, *Colloids Surf., A*, 2025, **709**, 136130.
32 S. Besra, S. Iaiche, K. Belakroum and S. Bergoug, *Solid State Commun.*, 2026, **409**, 116321.
33 T. V. Ha Luu, T. L. Nguyen, T. M. Hien Bach, N. T. Dung, N. N. Huy and H. P. Dang, *RSC Adv.*, 2025, **15**, 26552–26566.
34 N. Sakar, S. A. Akalin, A. Yavas, M. Zeyrek, P. Kose and S. Oguzlar, *J. Alloys Compd.*, 2025, **1021**, 179672.
35 S. Khan, D. S. Kim, M. Ullah, M. Sadiq, N. Muhammad, M. Khan, A. Noor and S. Qayyum, *Sci. Rep.*, 2025, **15**, 31947.
36 J. Wang, T. Zhang, X. Liu, L. Yang, J. Cao, Q. Wu, F. Wang, Y. Chen and M. Wei, *RSC Adv.*, 2025, **15**, 40174–40187.
37 R. Ghorbali, G. Essalah, A. Ghoudi, H. Guermazi, S. Guermazi, A. El Hdiy, H. Benhayoune, B. Duponchel, A. Oueslati and G. Leroy, *Ceram. Int.*, 2023, **49**, 33828–33841.
38 D. Thi Bich Hop, T. Quoc Tuan, N. Van Quang, N. Tu, H. Le Tien, M. T. Tran, T. Quang Vinh, N. Cong Tu, T. Ngoc Bach, V. D. Dao and P. Thi Lan Huong, *Ceram. Int.*, 2024, **50**, 17338–17353.
39 Z. Raad, U. Yahsi and L. Arda, *J. Alloys Compd.*, 2025, **1046**, 184736.
40 R. Sonkar, N. J. Mondal, B. Boro, M. P. Ghosh and D. Chowdhury, *J. Phys. Chem. Solids*, 2024, **185**, 111715.
41 F. M. Sanakousar, C. C. Vidyasagar, D. B. Shikandar, N. Mounesh, C. C. Viswanatha, G. Hosamani, K. Prakash and N. K. Manjunatha, *React. Chem. Eng.*, 2023, **8**, 2566–2591.
42 G. M. Fortes, A. L. da Silva, B. Ramos, J. Bettini, F. C. Fonseca, R. V. Gonçalves, O. Rodrigues Junior and D. Gouvea, *ACS Appl. Nano Mater.*, 2025, **8**, 2481–2492.
43 T. Ma, Y. Lu, S. Gao, H. Liu, J. Zhang, L. Ma, R. Wang and K. Wang, *Sep. Purif. Technol.*, 2025, **371**, 133337.
44 R. Zhang, J. Cui, H. Wang, Q. Liu, C. Wei and J. Luo, *J. Environ. Chem. Eng.*, 2025, **13**, 117252.
45 M. Aqeel, M. Rashid, M. Ikram, A. Haider, S. Naz, J. Haider, A. Ul-Hamid and A. Shahzadi, *Dalton Trans.*, 2020, **49**, 8314–8330.
46 A. Tekin, R. Aydın, Ü. Akın, O. Kahveci, A. Akkaya, H. Kara and B. Şahin, *Mater. Chem. Phys.*, 2025, **343**, 131009.
47 S. M. Sajjadi and G. Hossinzadeh, *Ceram. Int.*, 2024, **50**, 36271–36285.

48 I. Mansouri, F. Saib, S. Boulahlib, A. Laachachi, M. Özacar and Y. Bessekhouad, *Inorg. Chem. Commun.*, 2024, **162**, 112236.
49 B. L. Zhu, J. Hu, M. Xie, J. Wu and X. W. Shi, *Mater. Today Commun.*, 2023, **35**, 1–12.
50 K. M. Srinivasamurthy, C. Zhang, J. Gouda V, K. Bhaskar, I. Zhitomirsky, S. Y. Wu, V. Ganesh, I. S. Yahia, H. Algarni, K. Manjunatha and N. Basavegowda, *J. Energy Storage*, 2025, **114**, 115735.
51 L. Cao, Z. W. Kang, Q. Ding, X. Zhang, H. Lin, M. Lin and D. P. Yang, *Sci. Total Environ.*, 2020, **723**, 138008.
52 M. Dhanalakshmi and V. Losetty, *J. Water Process Eng.*, 2025, **70**, 106933.
53 H. Mahdhi, N. Haddad, Ș. Țălu, F. Ghribi, K. Djessas and Z. Ben Ayadi, *J. Alloys Compd.*, 2025, **1020**, 179291.
54 T. T. T. Le, T. H. Bui, H. P. Le, T. G. A. Pham, T. T. H. Pham, C. D. Truong and L. Lieu, *Appl. Surf. Sci.*, 2025, **700**, 163253.
55 H. Khaliq, M. Adnan, M. Usman, F. Shahzad, A. Nadeem, G. A. Shazly, G. A. Ashraf and Z. Zhao, *Mater. Sci. Semicond. Process.*, 2025, **192**, 109425.
56 M. Alsaiari, S. Afzal, A. Sultan, S. Shukrullah, M. Saleem, M. Yasin Naz, M. A. Rizk and M. Irfan, *ACS Omega*, 2024, **9**, 1977–1989.
57 M. Kaur, P. Hait and S. Basu, *RSC Adv.*, 2025, **15**, 37166–37182.
58 P. Yan, W. Cheng, Y. Qi, S. Chen, B. Liao and M. Ying, *Appl. Surf. Sci.*, 2026, **717**, 164805.
59 O. Haddad, A. A. Hssi, A. Soussi, N. Labchir, B. Smiri, M. Belmoubarik, I. A. Brahim, K. Abouabassi, R. Markazi, A. Elfanaoui and A. Ihlal, *Mater. Sci. Eng., B*, 2026, **324**, 118891.
60 D. Wilsonamalraj, P. Saravanan, A. D. Raj, S. Rahul, C. D. Savio, H. J. Prabhu, S. J. Sundaram, M. W. Alam, S. Sadaf and J. V. Kumar, *Inorg. Chem. Commun.*, 2026, **184**, 115894.
61 N. C. Hien, N. H. Thang, T. Mahmood, A. Pawlicka, M. Anwar, M. Munir, A. Ghafoor and T. L. A. Khoa, *RSC Adv.*, 2025, **15**, 22730–22744.
62 I. Aslam, C. Cao, M. Tanveer, M. H. Farooq, W. S. Khan, M. Tahir, F. Idrees and S. Khalid, *RSC Adv.*, 2015, **5**, 6019–6026.
63 V. Mariyappillai, C. Shiyamala, M. Tiffany, T. Abisheik, V. Pandiyan, A. K. Alanazi, P. Kalakonda, A. Thirumurugan, G. Sandoval-Hevia and K. Balu, *Colloids Surf., A*, 2025, **727**, 138212.
64 H. Yang, C. Ai, Y. Zhou, B. He, J. Zhang and J. Yu, *Artif. Photosynth.*, 2026, **2**, 53–66.
65 F. Andish-Lifshagerd, A. Habibi-Yangjeh, M. Habibi, M. Padervand and A. Khataee, *Colloids Surf., A*, 2025, **714**, 136584.
66 S. Zhuang, Y. Lei, F. Xue, T. Wei, J. Chu, M. Cui, Z. Zhang, R. Wei, J. Tang and X. Qiao, *Appl. Surf. Sci.*, 2025, **709**, 163840.
67 A. Ashraf, S. Rashid Tariq and G. Abbas Chotana, *Appl. Surf. Sci.*, 2025, **679**, 161251.
68 N. Leishangthem, T. S. Singh and N. M. Singh, *Inorg. Chem. Commun.*, 2025, **180**, 115048.
69 I. Ayman, M. Aadil, M. Shahid, A. Khalid, H. Samama, H. H. Somaily, M. F. Warsi and R. M. K. Mohamed, *Mater. Sci. Semicond. Process.*, 2024, **178**, 108462.
70 K. MohammedSaleh Katubi, K. Chaudhary, Z. A. Alrowaili, I. Shakir, M. F. Warsi, M. Shahid and M. S. Al-Buriahi, *Ceram. Int.*, 2025, **51**, 30113–30127.
71 N. Kousar, S. Rasheed, K. Yasmeen, A. R. Umar, M. H. Laiche, M. Masood, H. Muhammad and M. Hanif, *J. Water Process Eng.*, 2024, **58**, 104775.
72 A. Ayub, Z. A. Raza, M. I. Majeed, M. R. Tariq and A. Irfan, *Int. J. Biol. Macromol.*, 2020, **163**, 603–617.
73 M. A. Sayed, A. Mohamed, S. A. Ahmed, A. M. El-Sherbeeny, W. Al Zoubi and M. R. Abukhadra, *J. Photochem. Photobiol., A*, 2024, **456**, 115843.
74 E. R. Adly, M. S. Shaban, A. M. El-Sherbeeny, W. Al Zoubi and M. R. Abukhadra, *ACS Omega*, 2022, **7**, 31218–31232.
75 A. Moin, K. M. Younes, U. Fatima, S. M. D. Rizvi, A. S. A. Lila, A. A. AL-Shammary and M. F. Warsi, *J. Alloys Compd.*, 2025, **1020**, 179274.
76 F. M. A. Alzahrani, M. Aadil, S. T. Almutairi, H. H. Somaily, M. S. Al-Buriahi and M. F. Warsi, *Inorg. Chem. Commun.*, 2025, **182**, 115448.
77 A. Baillard, E. Appert, H. Roussel, J. M. Becht, V. Jacob and V. Consonni, *J. Environ. Chem. Eng.*, 2025, **13**, 115865.
78 J. Behin, P. Amiri and S. Ghabaee, *J. Environ. Manage.*, 2025, **389**, 126166.